

Lattice Identification and Separation: Theory and Algorithm ^{*}

Yuchen He [†] and Sung Ha Kang [‡]

Abstract

Motivated by lattice mixture identification and grain boundary detection, we present a framework for lattice pattern representation and comparison, and propose an efficient algorithm for lattice separation. We define new scale and shape descriptors, which helps to reduce the size of equivalence classes of lattice bases considerably. These finitely many equivalence relations are fully characterized by modular group theory. We construct the lattice space \mathcal{L} based on the equivalent descriptors and define a metric $d_{\mathcal{L}}$ to accurately quantify the visual similarities and differences between lattices. Furthermore, we introduce the Lattice Identification and Separation Algorithm (LISA), which identifies each lattice patterns from superposed lattices. LISA finds lattice candidates from the high responses in the image spectrum, then sequentially extracts different layers of lattice patterns one by one. Analyzing the frequency components, we reveal the intricate dependency of LISA's performances on particle radius, lattice density, and relative translations. Various numerical experiments are designed to show LISA's robustness against a large number of lattice layers, moiré patterns and missing particles.

1 Introduction

From material science to wallpaper pattern studies, there is a wide range of fruitful pattern research both in theory and applications. Earlier studies [9, 22, 29] categorize patterns by symmetries, such as invariance under reflections or rotations. Frieze and wallpaper groups are applied to identify periodic patterns in computer vision [68]. These pattern recognition typically involves two tasks: representation of regularities and automated classification [11], which are closely related.

Motivated by some of the current developments in material sciences [33, 62] and crystalline material image analysis [7, 8, 12, 30, 40, 70], we focus on two dimensional lattice, which plays major roles in crystallography [23, 60], sampling theory [50], ecology [66] and many others. For example, crystal structures of halite (NaCl) and gold (Au) have distinct scales (NaCl constant: 5.640Å [26]; Au constant: 4.065Å [19]), which explains their proprietary differences. There are considerable research on detecting (non-superposed) lattice patterns from images, e.g., using the peaks of the Fourier power spectrum to identify the lattice structure [41], and propagating an automatically suggested lattice pattern to the whole image by a tracking algorithm [49]. In [55], the authors associated the wallpaper groups with local affine transformations to cluster repeated elements, and Hays et al. [27] propose the higher-order affinities among potential texels to discover visually consistent lattices.

^{*}This research was supported by Simons Foundation grant 282311 and 584960.

[†]royarthur@gatech.edu, School of Mathematics, Georgia Institute of Technology 686 Cherry Street, Atlanta, GA 30332-0160 USA.

[‡]kang@math.gatech.edu, <http://people.math.gatech.edu/~kang/>, School of Mathematics, Georgia Institute of Technology 686 Cherry Street, Atlanta, GA 30332-0160 USA.

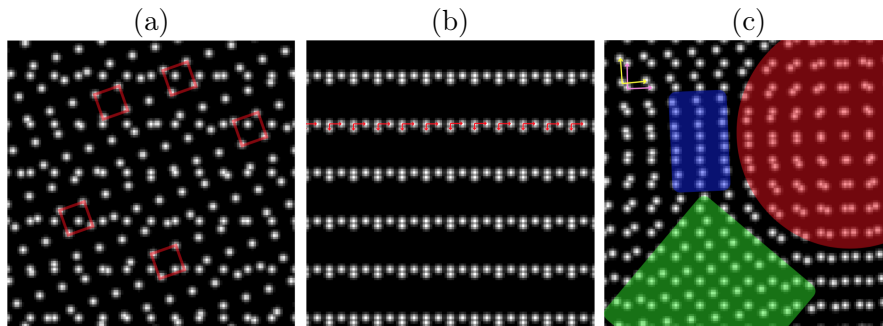


Figure 1: [Challenges of pattern separation] Each images have two lattices superposed. (a) Each red squares are units of one lattice, yet they have different interior patterns which can confuse the texture approach. (b) Using non-superposed lattice identification method, such as [49], wrong local feature L-shapes (the red arrows) can be identified. These red arrows do not correspond to true underlying lattices. (c) The pink and the yellow L-shapes on the top-left corner denote the true lattice components. There are three different types of Moiré patterns present (red, blue and green regions).

Our objective is to separate superposed lattices, which is a mixture of multiple two-dimensional lattices laid over another. This structure is referred to as a **superlattice** [34]. Subjects characterized by superlattices are explored in solid physics [25, 44, 67], surface waves [37, 58] and nonlinear optics [64]. One of the most significant discoveries in low-dimensional material sciences is the family of transition metal dichalcogenides (TMDs) [18, 47], such as MoS₂ [52] and WTe₂ [20]. A single sheet of TMD shows a superlattice structure: the top and the bottom are chalcogen atoms layers, and the middle is a transition metal atoms layer.

A clear definition of equivalent lattices is a cornerstone to classification. In many context [31, 54, 56], lattice is considered as an object who shares the structural characteristics with \mathbb{Z}^n , $n \in \mathbb{N}_{\geq 1}$, thus all the lattices are equivalent. Focusing on symmetries, the theory of wallpaper groups [22] distinguishes five types of lattices: square, rectangular, hexagonal, rhombic and parallelogrammic. Many works in grain boundary detection [12] use the lattice orientation to indicate distinct patterns. In this paper, we define equivalent lattices to be identical lattices up to translation. The scale, as well as rotational differences, are concerned.

Separating individual lattice pattern from a superlattice is challenging. First, it is difficult to determine the smallest unit, e.g., the texton [35]. Effective methods for non-superposed lattice, such as [39, 49] may fail, due to the interaction from different lattice layers. Figure 1 (a) shows when the textons of one lattice have inhomogeneous interiors, and (b) shows when local L-shapes [49] do not represent the correct underlying patterns. Secondly, superposed periodic patterns may produce new periodic structures, i.e., moiré patterns [4], which can confuse the identification process. (This phenomenon is exploited in some applications [6, 24].) Figure 1 (c) shows three different moiré patterns generated by two lattices, whose bases are represented by pink and red L-shapes in the left top corner. Thirdly, human supervision [14] can be unreliable. Psychological evidence [28, 35, 63, 65] prove that visual search can be interfered by similarities, e.g., less than 15° of rotational differences between targets and background increases errors [63], and small differences in densities can interfere target identification [35].

In this paper, we first establish a framework to model and compare equivalent classes of

lattices by constructing the **lattice space** \mathcal{L} equipped with a new metric $d_{\mathcal{L}}$. From the positive minimal bases [61], we derive a new lattice representation using scale and shape descriptors on complex manifolds. Our lattice space consists of equivalent classes of descriptors which represents distinct lattice patterns up to translation. Building upon the Poincaré metric [21], a metric structure is then assigned to the lattice space.

We propose a new Lattice Identification and Separation Algorithm (**LISA**). It sequentially extracts lattice patterns from a superlattice image without any prior knowledge of the number of layers. The main idea behind LISA is to measure the periodicities globally by Fourier transform. For higher accuracy of estimating lattice bases, we exploit the Fourier Slice Theorem [41]. By evaluating pairs of peaks on the power spectrum, the optimal lattice structure is found. We use a correcting step to obtain a stable estimation. The proposed method is designed to handle the moiré effect, excessive density, and inhomogeneous texture interior. We analytically study the properties of LISA. In particular, we reveal the effects of particle radius, lattice density and relative translations on LISA’s performances, and show that LISA is robust against Gaussian perturbation with bounded variation.

Main contributions of this paper are:

1. Introduction of the lattice descriptors and a lattice metric space, which gives a unifying representation for lattices and a tool to measure the visual differences and similarities between lattices.
2. Proposal for a new efficient lattice identification and separating algorithm. Our method does not require supervision, any prior knowledge of the lattices nor the number of layers. We provide analytical studies on the construction, efficiency, and robustness of the algorithm.

This paper is organized as follows. In Section 2, we present a typical notion of the lattice, state assumptions of the image, and review definitions as well as basic concepts. In Section 3, we introduce and study the descriptors by exploiting minimal bases and modular groups. The lattice space and its natural metric structure are defined in Section 4. We propose our algorithm LISA in Section 5 with analysis on properties of LISA starting in Section 5.3. Various numerical experiments are presented in Section 6. We conclude the paper with remarks in section 7, followed by Appendix including more discussion about sub-lattices and parent-lattices, and a pseudo-code computing lattice metric.

2 Preliminaries and Notations

A typical definition of lattice starts from two linearly independent vectors, b_1 and b_2 as basis. A lattice is a set of linear combination of these basis with integer coefficients. In two dimensional space, we utilize complex notation, $b_j = x_j + iy_j \in \mathbb{C}$, $x_j, y_j \in \mathbb{R}$, $j = 1, 2$, for simplicity.

Definition 2.1 (2D Lattice, Basis). Given a pair of complex numbers $(b_1, b_2) \in \mathbb{C}^2$ satisfying $b_1 \neq 0$ and $\text{Im}(b_2/b_1) \neq 0$, a 2D lattice determined by (b_1, b_2) is defined as the set:

$$\Lambda(b_1, b_2) = \{k_1 b_1 + k_2 b_2 \mid k_1, k_2 \in \mathbb{Z}\},$$

and the pair (b_1, b_2) is called a basis for $\Lambda(b_1, b_2)$.

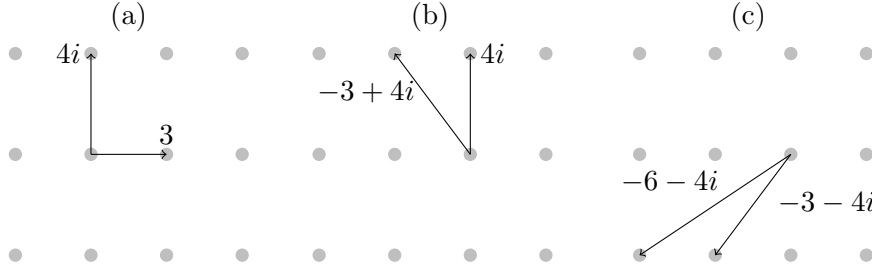


Figure 2: [Equivalent lattice and minimal bases] (a) $\Lambda(3, 4i)$, (b) $\Lambda(4i, -3 + 4i)$, and (c) $\Lambda(-3 - 4i, -6 - 4i)$ are all equivalent. (a) is a minimal basis: $|\operatorname{Re}(\frac{4i}{3})| = 0 < \frac{1}{2}$. (b) is not minimal: $|\operatorname{Re}(\frac{-3+4i}{4i})| = 1 > \frac{1}{2}$, and (c) is not positive: $\operatorname{Im}(\frac{-6-4i}{-3-4i}) = -\frac{12}{25} < 0$.

The condition $\operatorname{Im}(b_2/b_1) \neq 0$ represents two vectors b_1 and b_2 being linearly independent. For any lattice $\Lambda(b_1, b_2)$, by reordering or multiplying -1 if necessary, we assume that $|b_1| \leq |b_2|$, and $\operatorname{Im}(b_2/b_1) > 0$, i.e. the basis (b_1, b_2) is positive. The key to distinguishing lattices depends on the equivalent bases.

Definition 2.2 (Equivalent Bases). Let (b_1, b_2) and $(b'_1, b'_2) \in \mathbb{C}^2$. If $\Lambda(b_1, b_2) = \Lambda(b'_1, b'_2)$, then (b_1, b_2) and (b'_1, b'_2) are called a pair of equivalent bases for $\Lambda(b_1, b_2)$.

Given two bases (b_1, b_2) and (b'_1, b'_2) , they are equivalent if and only if the matrix

$$A = \begin{bmatrix} \operatorname{Re}(b'_1) & \operatorname{Im}(b'_1) \\ \operatorname{Re}(b'_2) & \operatorname{Im}(b'_2) \end{bmatrix} \begin{bmatrix} \operatorname{Re}(b_1) & \operatorname{Im}(b_1) \\ \operatorname{Re}(b_2) & \operatorname{Im}(b_2) \end{bmatrix}^{-1}$$

has integer entries and the determinant is ± 1 . The definition of lattice using linearly independent vectors is natural and intuitive, yet, lacks a clear way to define equivalence classes nor has a simple measure for lattice comparison.

Another important notion is **minimal basis** [57]. A basis (b_1, b_2) is minimal if $\max(|b_1|, |b_2|) \leq |b_1 \pm b_2|$. Any pair of positive basis can be efficiently transformed to an equivalent minimal basis using the Positive Gauss reduction algorithm [61]. It takes a positive basis (b_1, b_2) as the input. While $|b_2| < |b_1|$, repeat the following until stabilization: $(b_1, b_2) = (b_2, -b_1)$, $q = \lfloor \operatorname{Re}(b_1/b_2) \rfloor$, and $b_2 = b_2 - qb_1$. The output is a minimal basis. Figure 2 demonstrates three different bases generating an identical lattice, and one can check that (a) $(3, 4i)$ has the shortest components among all the equivalent bases.

We assume that the given image $U : \mathbb{R}^2 \rightarrow [0, 1]$ contains N lattices $\{\mathcal{T}_{\mu_j} \Lambda_j := \mathcal{T}_{\mu_j} \Lambda_j(b_{j,1}, b_{j,2})\}_{j=1}^N$,

$$U(x, y) = \max_{j=1, \dots, N} \mathcal{T}_{\mu_j} \Lambda_j(b_{j,1}, b_{j,2}) + R(x, y), \quad (x, y) \in \mathbb{R}^2. \quad (1)$$

Here $\mathcal{T}_{\mu} \Lambda(b_1, b_2)$ denotes a lattice translated from 0 by $\mu \in \mathbb{C}$, and R is the residual term. For visualization of lattice points, we put a point spread function (PSF) of Gaussian G_{σ} with standard deviation σ to each lattice point location [1], i.e.

$$\mathcal{T}_{\mu} \Lambda(b_1, b_2) = \sum_{k_1, k_2 \in \mathbb{Z}} G_{\sigma} * \delta(k_1 b_1 + k_2 b_2 + \mu - x - iy), \quad (x, y) \in \mathbb{R}^2,$$

where δ is the Dirac function on \mathbb{C} defined by $\delta(x + iy) = 1$ if $x + iy = 0$, and $\delta(x + iy) = 0$ otherwise. All the visible particles are assumed to be homogeneous, i.e., even if multiple lattice points overlapping at the same location, the height is bounded by 1. This condition is ensured by the normalization in section 5.

To capture the periodicities of the lattice pattern, we utilize the Fourier and Radon transforms. In complex representation, arguments of the bases are important features and polar coordinate is more efficient in locating the peaks. For example, in Cartesian coordination, for a peak (ξ, ν) in the frequency domain, the argument estimation error $\Delta\theta$ at θ and the spatial discretization $\Delta\xi, \Delta\nu$ are related by $|\Delta\theta| \approx \left| \frac{\xi\Delta\nu - \nu\Delta\xi}{\xi^2 + \nu^2} \right|$. To control $\Delta\theta$, the grid size must vary according to peak locations. We exploit the Fourier Slice Theorem [15] to switch the coordinate system and use polar coordinates in this paper.

Theorem 2.3 (Fourier Slice Theorem). *Consider a function $f : \mathbb{R}^2 \rightarrow \mathbb{R}$, and denote \hat{f} as the Fourier transform, then:*

$$\hat{f}(\gamma \cos \alpha, \gamma \sin \alpha) = \widehat{\mathcal{R}_\alpha[f]}(\gamma), \forall \gamma \in \mathbb{R}, \alpha \in [0, \pi),$$

where $\mathcal{R}_\alpha[f](\gamma) := \mathcal{R}[f](\gamma, \alpha)$, and $\mathcal{R}[f]$ is the radon transform of f defined by:

$$\mathcal{R}[f](\gamma, \alpha) := \int_{-\infty}^{+\infty} f(\gamma \cos \alpha - t \sin \alpha, \gamma \sin \alpha + t \cos \alpha) dt, \gamma \in \mathbb{R}, \alpha \in [0, \pi).$$

To construct a metric space, we review the following concepts [16] to be used in Section 4.

Definition 2.4 (Quotient pseudometric). Suppose (X, D) is a metric space, and \sim is an equivalence relation defined on X . Then the quotient pseudometric \bar{D} for X/\sim is defined as follows:

$$\bar{D}([x], [y]) = \inf\{D(p_1, q_1) + \dots + D(p_n, q_n)\},$$

where \inf is taken over all finite sequences p_1, \dots, p_n and q_1, \dots, q_n in X such that $[p_1] = [x]$, $[q_n] = [y]$ and $[p_{i+1}] = [q_i]$, $i = 1, 2, \dots, n - 1$.

The spaces in our work are Kolmogorov spaces, i.e., for every pair of distinct points, each has a neighborhood not containing the other. Hence all the quotient pseudometrics in this paper are in fact metrics.

Definition 2.5 (Product Metric). Suppose $(X_1, d_1), (X_2, d_2), \dots, (X_n, d_n)$ are metric spaces, and D is an Euclidean norm on \mathbb{R}^n , then the product metric D_{d_1, \dots, d_n} associated with d_1, \dots, d_n for the space $X_1 \times \dots \times X_n$ is defined as:

$$D_{d_1, \dots, d_n}((x_1, \dots, x_n), (y_1, \dots, y_n)) = D((d_1(x_1, y_1), \dots, d_n(x_n, y_n))).$$

Remark 2.6. The formal definition of minimal basis that involves successive minima can be found in [57]. The minimal basis is a special case of the reduced basis for a lattice in general dimension. Variations of this notion include well-known Minkowski-reduced basis [42, 43], generalized Gauss-reduced basis [51], Hermite-Korkine-Zolotarev-reduced basis [17, 36], and Lenstra-Lenstra-Lovász-reduced basis [38]. They consider different relaxations, since finding the shortest vector using L_2 -norm is NP-hard for randomized reductions [2].

Remark 2.7. Vallée and Vera [61] also include discussions about acute bases, which is the situation where $\text{Re}(b_2/b_1) \geq 0$. If (b_1, b_2) is a positive basis, then the orientation is guaranteed, but it is not necessary that b_1 and b_2 have acute angle. If the basis is acute, then it loses the orientability. In this paper, we prioritize the orientability, thus focus on positive bases.

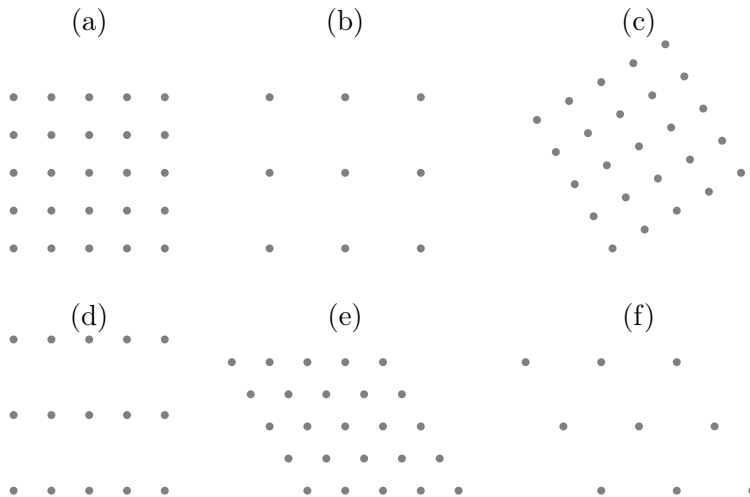


Figure 3: [Descriptors β and ρ] (a) $\Lambda\langle 1, i \rangle$, (b) $\Lambda\langle 2, i \rangle$, (c) $\Lambda\langle e^{i\pi/6}, i \rangle$, (d) $\Lambda\langle 1, 2i \rangle$, (e) $\Lambda\langle 1, e^{2\pi i/3} \rangle$, and (f) $\Lambda\langle 2, e^{2\pi i/3} \rangle$. From (a) to (b), only β changed from 1 to 2. From (a) to (c), β is rotated. From (a) to (d), ρ changed from i to $2i$. From (a) to (e), ρ is rotated,. From (a) to (f), both β changed and ρ rotated.

3 New Lattice Representation: descriptors β and ρ

We explore a new representation for a lattice using a pair of complex numbers $(\beta, \rho) \in \mathbb{C}^2$, which we call descriptors. These are derived from the positive minimal bases [61], and the key observation is that a lattice is realized as a transformed unit lattice. Transformations such as zoom-in, zoom-out and rotation are encoded in the scale descriptor β , and sheering, skew elongation or shrinking are controlled by the shape descriptor ρ . One of the advantages of descriptors is that, compared to the Definition 2.1, the number of equivalent representations is dramatically reduced from infinite to only a few. These equivalence relations can be fully characterized by exploiting the modular group theory [5]. Descriptors modulo these relations are used as elements for the lattice space in Section 4.

Definition 3.1 (Scale and Shape Descriptor). Given a lattice $\Lambda(b_1, b_2)$ where (b_1, b_2) is a minimal basis, we define:

$$\text{Scale descriptor: } \beta = b_1;$$

$$\text{Shape descriptor: } \rho = b_2/b_1.$$

We denote $\Lambda\langle \beta, \rho \rangle$ to be a lattice, which is spanned by β and $\beta\rho$, i.e. $\Lambda\langle \beta, \rho \rangle = \Lambda(\beta, \beta\rho)$.

Figure 3 illustrates various effects of changing β and ρ . From (a) to (b), only β changed from 1 to 2, and from (a) to (c), β is rotated. From (a) to (d) ρ changed from i to $2i$, and from (a) to (e), ρ is rotated. From (a) to (f) both β changed and ρ rotated. Varying the scale descriptor β corresponds to zooming and rotations, while the shape descriptor ρ corresponds to sheering, skew elongation and skew shrinking. More importantly, equivalent bases determine a simple algebraic relation between their descriptors.

Proposition 3.2 (Necessary condition). *If two lattices $\Lambda\langle\beta, \rho\rangle$ and $\Lambda\langle\beta', \rho'\rangle$ are equivalent, then there exists $k_i \in \mathbb{Z}$, $i = 1, 2, 3, 4$ with $k_1k_4 - k_2k_3 = 1$, such that the following hold:*

$$\beta' = e^{i\text{Arg}(k_1+k_2\rho)}\beta, \text{ and} \quad (2)$$

$$\rho' = (k_3 + k_4\rho)/(k_1 + k_2\rho). \quad (3)$$

Proof. Note that $\Lambda\langle\beta, \rho\rangle = \Lambda\langle\beta', \rho'\rangle$ if and only if there is a unimodular matrix $U = \begin{bmatrix} k_1 & k_2 \\ k_3 & k_4 \end{bmatrix}$, $k_i \in \mathbb{Z}$, $i = 1, 2, 3, 4$, such that $U \begin{bmatrix} b_1 \\ b_2 \end{bmatrix} = \begin{bmatrix} b'_1 \\ b'_2 \end{bmatrix}$, where $b_1 = \beta$, $b_2 = \beta\rho$, $b'_1 = \beta'$ and $b'_2 = \beta'\rho'$ are the associated bases respectively. From the matrix multiplication, (3) follows immediately. Because the bases are minimal, $|b_1| = |b'_1|$ implies $b'_1 = e^{i\theta}b_1$ for some $\theta \in [0, 2\pi]$. Combining this with $b'_1 = k_1b_1 + k_2b_2$ gives $k_1 + k_2\rho = e^{i\theta}$, thus $\theta = \text{Arg}(k_1 + k_2\rho)$ and (2) follows. In addition, since (b_1, b_2) and (b'_1, b'_2) are positive, $\det U = k_1k_4 - k_2k_3 = 1$. \square

In the following, we apply the modular group theory to prove the converse of Proposition 3.2, hence whether two descriptors generate an identical lattice can be easily determined. As a preparation, we state a lemma.

Lemma 3.3. *The converse of Proposition 3.2 holds if*

$$|k_1 + k_2\rho| = 1.$$

Proof. Denote $c = \frac{1}{|k_1+k_2\rho|} = \frac{e^{i\text{Arg}(k_1+k_2\rho)}}{k_1+k_2\rho}$, then from (2), we have $b'_1 = \beta' = c(k_1 + k_2\rho)\beta = c(k_1b_1 + k_2b_2)$. Notice that (3) reads $b'_2 = b'_1 \frac{k_3+k_4\rho}{k_1+k_2\rho} = c(k_1 + k_2\rho)\beta \frac{k_3+k_4\rho}{k_1+k_2\rho} = c(k_3b_1 + k_4b_2)$. The lemma is thus proved. \square

Since the equivalence condition (2) shows the dependency of β on ρ , we start with the details of shape descriptor ρ in (3).

3.1 Equivalence class of shape descriptor ρ

The definition 3.1 of the new descriptors starts from the minimal basis notation (see Section 2). Using basic geometry, it is straightforward to show that the definition of the minimal basis is equivalent to the ratio $\rho = b_2/b_1$ belonging to the following region:

$$\mathcal{P} := \{z \in \mathbb{C} \mid |z| \geq 1, |\text{Re}(z)| \leq \frac{1}{2}, \text{Im}(z) > 0\} \subset \mathbb{C}. \quad (4)$$

Figure 4 shows \mathcal{P} as the shaded region in (a) with the boundary. As an example, we consider vectors ρ , ρ' and ρ'' which are the shape descriptors for the bases $\Lambda(3, 4i)$, $\Lambda(4i, -3 + 4i)$, and $\Lambda(-3 - 4i, -6 - 4i)$ in Figure 2 (a)-(c) in order. These represent the same lattice, while ρ from $\Lambda(3, 4i)$ is a minimal basis.

The equivalence condition (3) can be viewed as a transformation defined on the upper-half plane $\mathcal{H} = \{z \mid \text{Im}(z) > 0\}$ restricted to \mathcal{P} . It is expressed as:

$$z \mapsto \frac{k_3 + k_4z}{k_1 + k_2z}, \quad \{k_i\}_{i=1}^4 \subset \mathbb{Z}, \text{ such that } k_1k_4 - k_2k_3 = 1, \forall z \in \mathcal{H},$$

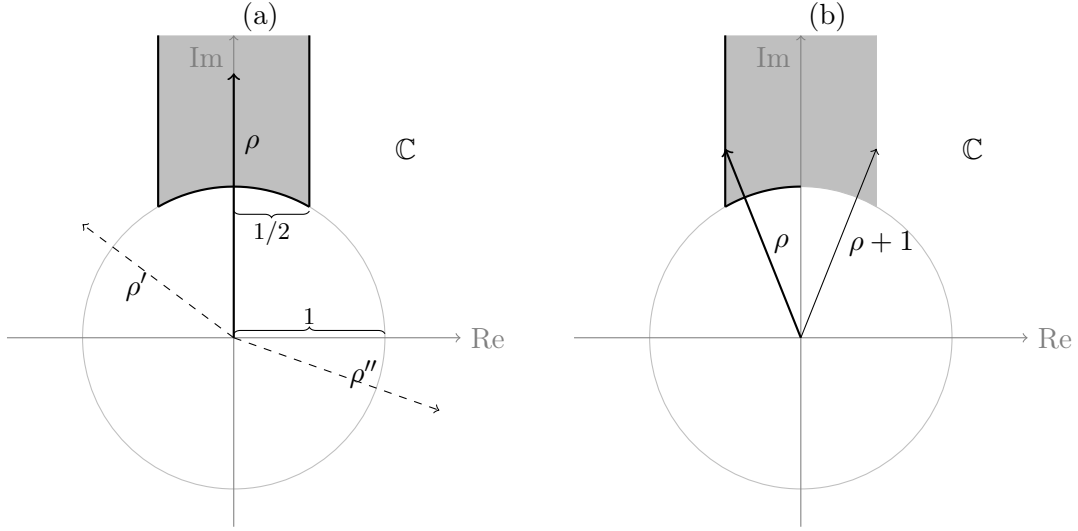


Figure 4: The shaded region in (a) with the boundary is \mathcal{P} . Vectors ρ , ρ' and ρ'' are the shape descriptors for the bases $\Lambda(3, 4i)$, $\Lambda(4i, -3 + 4i)$, and $\Lambda(-3 - 4i, -6 - 4i)$ in Figure 2 (a)-(c) in order. All represents the same lattice, while ρ for $\Lambda(3, 4i)$ is a minimal basis. (b) A fundamental set of the modular group Γ acting on the upper half plane \mathcal{H} . If $\text{Re}(\rho) = -1/2$, ρ and $\rho + 1$ are in the same orbit.

Each function of this form is a special case of Möbius transforms, and the set of these transformations under function composition gives the well-known modular group [5], denoted by Γ . The elements in Γ act on the upper half plane \mathcal{H} naturally. Within the context of group actions, the equivalence condition (3) indicates that equivalent ρ live in the same orbit of Γ -actions.

The invocation of the modular group Γ also reveals the significance of the region \mathcal{P} defined in (4). This \mathcal{P} minus half of its boundary:

$$\mathcal{P} \setminus (\{z \in \mathcal{H} \mid \text{Re}(z) = \frac{1}{2}\} \cup \{z \in \mathcal{H} \mid 0 < \text{Re}(z) < \frac{1}{2}, |z| = 1\}),$$

is a fundamental set for Γ -actions [5]. See Figure 4 (b). Every element in the fundamental set is a representative of one and only one orbit, and every orbit corresponds to a unique representative. No two shape descriptors in the difference set are equivalent. This result provides a key insight that equivalent shape descriptors only occur on the boundary of \mathcal{P} .

Following the approach of Alperin on the modular group [3], we can enumerate all the classes of equivalent shape descriptors systematically. Any Γ -action is a composition of a finite sequence of two basic transformations: translation T and inversion followed by reflection S . For example, if we denote:

$$T : z \mapsto z + 1, \text{ and } S : z \mapsto -1/z, \text{ for any } z \in \mathcal{H},$$

then any element in Γ can be written as $S^{k_1}T^{l_1}S^{k_2}T^{l_2} \dots S^{k_m}T^{l_m}$ for some $k_j \in \{0, 1\}$, $l_j \in \mathbb{Z}$, and $j = 1, 2, \dots, m$, where $m \in \mathbb{N}$. Focusing on the sequences of S and T acting on \mathcal{P} , we arrive at a full characterization of equivalence classes of shape descriptors.

Proposition 3.4. *Given a shape descriptor $\rho \in \mathcal{P}$, we list all the shape descriptors equivalent to it, based on the location of ρ in \mathcal{P} as follows:*

Location of ρ	All the equivalent shape descriptors
$\{z \in \mathcal{P} \mid z > 1, \operatorname{Re}(z) < 1/2\}$	ρ
$\{z \in \mathcal{P} \mid \operatorname{Re}(z) = -1/2, z > 1\}$	$\rho, T\rho$
$\{z \in \mathcal{P} \mid \operatorname{Re}(z) = 1/2, z > 1\}$	$\rho, T^{-1}\rho$
$\{z \in \mathcal{P} \mid z = 1, 0 \leq \operatorname{Re}(z) < 1/2\}$	$\rho, S\rho$
$e^{i2\pi/3}$	$\rho, S\rho, T\rho, T^{-1}S\rho, ST\rho, TST\rho$
$e^{i\pi/3}$	$\rho, S\rho, T^{-1}\rho, TS\rho, ST^{-1}\rho, STS\rho$

Geometrically, the small sizes of equivalence classes come from the restriction, that both ρ and ρ' belong to \mathcal{P} . In effect, the fundamental principle lurking behind the reduction is the uniqueness of successive minima of a finite dimensional lattice. This requires that the transformations relating two shape descriptors must preserve norm, and they form a proper subset of the modular group.

Remark 3.5. Relating to wallpaper groups [22], the notion of shape descriptor ρ is compatible with the 5 classes of lattices. For a lattice $\Lambda\langle\beta, \rho\rangle$, if $\rho = \pm\frac{1}{2} + i\frac{\sqrt{3}}{2}$, then it is hexagonal; if $\rho = i$, then it is square; if $\operatorname{Re}(\rho) = 0$, then it is rectangular; if $|\operatorname{Re}(\rho)| = \frac{1}{2}$ or $|\rho| = 1$, then it is rhombic; otherwise, it is parallelogrammic. The shape descriptor ρ recognizes finer differences, and with the scale descriptor β , they represents all lattice patterns up to translation.

3.2 Equivalence class of scale descriptor β

The condition (2) shows the dependency of equivalence relations of scale descriptors β on that of shape descriptors ρ . The choice of Γ -action that achieves equivalence relation between ρ and ρ' restricts the angles between β and its equivalent elements. Every Γ action is associated with a matrix $\begin{bmatrix} k_4 & k_3 \\ k_2 & k_1 \end{bmatrix}$, whose entries in the first row are the coefficients in the numerator in (3), and those in the second row the coefficients in the denominator. Corresponding to the nontrivial actions in Proposition 3.4, the matrix representations are:

$$T = \begin{bmatrix} 1 & 1 \\ 0 & 1 \end{bmatrix}, T^{-1} = \begin{bmatrix} 1 & -1 \\ 0 & 1 \end{bmatrix}, S = \begin{bmatrix} 0 & -1 \\ 1 & 0 \end{bmatrix}, T^{-1}S = \begin{bmatrix} -1 & -1 \\ 1 & 0 \end{bmatrix}, TS = \begin{bmatrix} 1 & -1 \\ 1 & 0 \end{bmatrix},$$

$$TST = \begin{bmatrix} 1 & 0 \\ 1 & 1 \end{bmatrix}, ST = \begin{bmatrix} 0 & -1 \\ 1 & 1 \end{bmatrix}, ST^{-1} = \begin{bmatrix} 0 & -1 \\ 1 & -1 \end{bmatrix}, STS = \begin{bmatrix} -1 & 0 \\ 1 & -1 \end{bmatrix}.$$

This entire list of possible Γ -actions that relate equivalent shape descriptors contains critical information. First, observe that for any $\rho \in \mathcal{P}$, the corresponding Γ -actions in Proposition 3.4 always satisfy $|k_1 + k_2\rho| = 1$, where the action is expressed as a matrix $\begin{bmatrix} k_4 & k_3 \\ k_2 & k_1 \end{bmatrix}$. Therefore, combining Proposition 3.4 and Lemma 3.3 yields our fundamental result.

Theorem 3.6 (Equivalent descriptors). *Two lattices $\Lambda\langle\beta, \rho\rangle$ and $\Lambda\langle\beta', \rho'\rangle$ are equivalent **if and only if** there exists $k_i \in \mathbb{Z}$, $i = 1, 2, 3, 4$ with $k_1k_4 - k_2k_3 = 1$, such that the following hold:*

$$\begin{aligned}\beta' &= e^{i\text{Arg}(k_1+k_2\rho)}\beta, \text{ and} \\ \rho' &= (k_3 + k_4\rho)/(k_1 + k_2\rho).\end{aligned}$$

Second, this list allows us to summarize all the variants of (2).

Proposition 3.7. *Given a scale descriptor $\beta \in \mathbb{C} \setminus \{0\}$ and two shape descriptors $\rho, \rho' \in \mathcal{P}$. If ρ and ρ' are equivalent using the Γ -actions in the left column of the following table, then all the scale descriptors that satisfy the scale condition with β are listed in the right column correspondingly.*

Γ -actions	Scale condition satisfied with
I, T, T^{-1}	$\pm\beta$
$S, T^{-1}S, TS$	$\exp(\pm i\text{Arg}(\rho))\beta$
TST, ST	$\exp(\pm i\text{Arg}(1 + \rho))\beta$
ST^{-1}, STS	$\exp(\pm i\text{Arg}(1 - \rho))\beta$

Using the matrix representation, we can identify the group of Möbius transforms with the projective general linear group $\text{PGL}_2(\mathbb{C})$, and the modular group with the projective special linear group $\text{PSL}_2(\mathbb{Z})$. In this sense, Subsection 3.1 and 3.2 establish the connection between equivalent lattices with the subgroup $\text{PSL}_2(\mathbb{Z}) \leq \text{PGL}_2(\mathbb{C})$. In the appendix, we extend similar algebraic correspondence to link sub-lattices with monoids and find that it is intrinsically hard to search for a particular sub-lattice or a parent-lattice of a given lattice systematically.

4 New Definition of Lattice Space and Metric

Using the descriptors, we present the lattice space \mathcal{L} equipped with a metric $d_{\mathcal{L}}$. The equivalence relations allow every lattice pattern be uniquely represented by a point in this space \mathcal{L} .

Definition 4.1 (Lattice Space). Let \mathcal{P} be the set of shape descriptors ρ (4), and $\mathcal{K} := \mathbb{C} \setminus \{0\}$ be the set of scale descriptors β . The lattice space \mathcal{L} is defined as follows:

$$\mathcal{L} = (\mathcal{K} / \sim_1 \times \mathcal{P} / \sim_2) / \sim_3, \quad (5)$$

where the three equivalence relations are:

1. $\beta \sim_1 -\beta$, $\forall \beta \in \mathcal{K}$, i.e., $\Lambda\langle\beta, \rho\rangle = \Lambda\langle-\beta, \rho\rangle$
2. $\rho \sim_2 \rho'$, $\forall \rho, \rho' \in \mathcal{P}$, i.e., $\Lambda\langle\beta, \rho\rangle = \Lambda\langle\beta, \rho'\rangle$, for $\text{Im}(\rho) = \text{Im}(\rho')$ and $|\text{Re}(\rho)| = |\text{Re}(\rho')| = 1/2$,
3. $\langle[\beta]_1, [\rho]_2\rangle \sim_3 \langle[\beta\rho]_1, [-1/\rho]_2\rangle$, $\forall \beta \in \mathcal{K}$, $\forall \rho \in \mathcal{P}$, i.e., $\Lambda\langle\beta, \rho\rangle = \Lambda\langle\beta\rho, -1/\rho\rangle$, for $|\rho| = 1$,

and \mathcal{L} has the induced topology. We denote $[\beta, \rho]$ as an element in \mathcal{L} considering the equivalence relations.

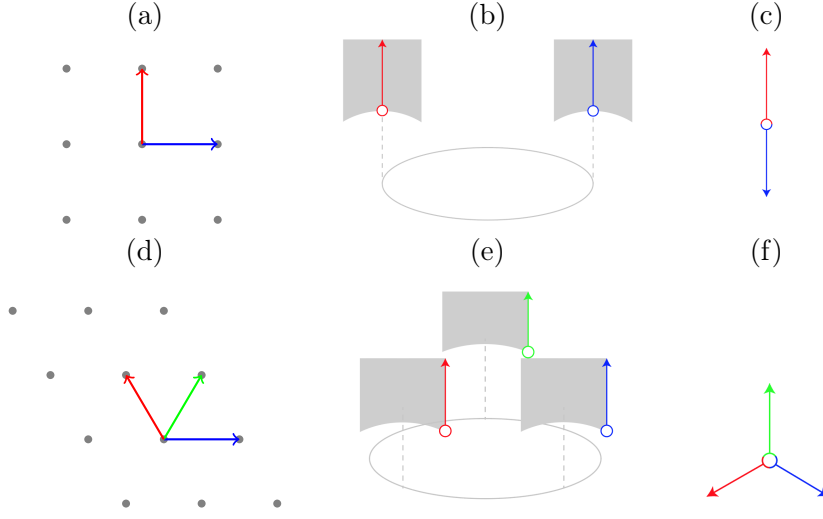


Figure 5: [Examples of subspaces of \mathcal{L}] (a) A square lattice $\Lambda\langle\beta, i\rangle$. The red and blue arrows indicate two directions. Stretching along them represents two different families of lattices. They form a subspace of \mathcal{L} shown in (b), and it is homeomorphic to \mathbb{R} as in (c). The second row (d) shows a lattice $\Lambda\langle\beta, e^{i\pi/3}\rangle$. Stretching along the three marked directions generates three distinct families of lattices. (e) is the subspace they form in \mathcal{L} , which is homeomorphic to (f).

The first equivalence relation, \mathcal{K}/\sim_1 , consists of scale descriptors β up to sign, which is equivalent to only considering the upper-half plane \mathcal{H} union the positive real axis. The second equivalence relation comes from the region \mathcal{P} in Figure 4, which is naturally turned into a hyperbolic surface when the Poincaré metric [21] is applied. Gluing together the left and right boundaries of \mathcal{P} , \mathcal{P}/\sim_2 becomes homeomorphic to a truncated cylindrical surface. The third equivalence relation \sim_3 represents a particular case when the basis vectors have an identical length, i.e. $|b_1| = |b_2|$. In such a case, there are a number of different representations for the same lattice pattern. This introduces many different paths for length computation, and these different paths are carefully considered for metric definition below.

To give more insights into the topologies of lattice space \mathcal{L} , we present a couple of special types of lattices. The top row of Figure 5, (a) illustrates the set of rectangular lattices $\Lambda\langle\beta, i\rangle$ with the red and blue lines. It is homeomorphic to the real axis \mathbb{R} as shown in (b) and (c). The midpoint of which represents the square lattice $\Lambda\langle\beta, i\rangle$. A point $r > 0$ on the positive side (the red half in (b)) is a lattice of the form $\Lambda\langle\beta, i+r\rangle$, and a point $r < 0$ on the negative side (the blue half in (b)) is a lattice of the form $\Lambda\langle\beta e^{i\pi/2}, i-r\rangle$. They correspond to stretching a square lattice in two directions in (c), resulting two families of distinct lattices, i.e., a bifurcate structure in \mathcal{L} . Another example is the union of hexagonal lattices and rhombic lattices whose shape descriptors have magnitude greater than 1. Take its subset of lattices having scale descriptors equivalent to β , as the union of the red, green and blue lines in Figure 5 (d). This is homeomorphic to (e), which consists of three half lines glued together at their endpoints. They represent three directions along which stretching a hexagonal lattice gives three distinct families of lattices, rendering a trifurcate structure in \mathcal{L} .

On \mathcal{L} , we now construct a metric structure starting from defining a metric D on \mathcal{K}/\sim_1

$\times \mathcal{P} / \sim_2$. Given any two descriptor pairs $(\beta, \rho), (\beta', \rho') \in \mathcal{K} \times \mathcal{P}$, we define

$$D((\beta, \rho), (\beta', \rho')) = \sqrt{d_{\mathcal{K}}(\beta, \beta')^2 + d_{\mathcal{P}}(\rho, \rho')^2}, \quad (6)$$

where equivalence relations will be incorporated into the definition of $d_{\mathcal{K}}$ and $d_{\mathcal{P}}$ respectively. Let $D_{\mathcal{K}}$ be a simple metric on \mathcal{K} , which separates the length differences and angle differences as:

$$D_{\mathcal{K}}(\beta, \beta') = \sqrt{w(|\beta| - |\beta'|)^2 + (1-w)(\cos^{-1} \frac{\operatorname{Re}(\beta\bar{\beta}')}{|\beta||\beta'|})^2}.$$

Here w is a parameter which adjusts the sensitivity between angle and length. We use $w = 0.05$ through out this paper. The quotient metric on \mathcal{K} is then defined as:

$$d_{\mathcal{K}}(\beta, \beta') = \min\{D_{\mathcal{K}}(\beta, \beta'), D_{\mathcal{K}}(-\beta, \beta')\}.$$

Let $D_{\mathcal{P}}$ be the well-known Poincaré metric [21] restricted to \mathcal{P} computed via:

$$D_{\mathcal{P}}(\rho, \rho') = 2 \ln \frac{|\rho - \rho'| + |\rho - \bar{\rho}'|}{2\sqrt{\operatorname{Im}(\rho)\operatorname{Im}(\rho')}},$$

and the corresponding quotient metric be

$$d_{\mathcal{P}}(\rho, \rho') = \min\{D_{\mathcal{P}}(\rho, \rho'), D_{\mathcal{P}}(\rho - 1, \rho'), D_{\mathcal{P}}(\rho + 1, \rho')\}.$$

To complete the definition of $d_{\mathcal{L}}$, we consider the third equivalence relation \sim_3 . This corresponds to a particular class of lattices whose minimal bases satisfy: $|b_1| = |b_2|$. They have multiple representations in the lattice space \mathcal{L} using the pairs of descriptors (β, ρ) . When considering all the path connecting any two points $(\beta, \rho), (\beta', \rho') \in \mathcal{L}$, we must consider the path passing through points in $E = \{(\beta, \rho) \mid \beta \in \mathcal{K}, |\rho| = 1, \rho \in \mathcal{P}\}$ for the third equivalence relation. There are eight such cases:

$$\begin{aligned} D_1 &: (\beta, \rho) \rightarrow (\beta', e^{i\phi}) \rightarrow (\beta', \rho'), \\ D_2 &: (\beta, \rho) \rightarrow (e^{i\phi'}\beta', -e^{-i\phi'}) \dashrightarrow (\beta', e^{i\phi'}) \rightarrow (\beta', \rho'), \\ D_3 &: (\beta, \rho) \rightarrow (\beta, e^{i\phi}) \rightarrow (\beta', \rho'), \\ D_4 &: (\beta, \rho) \rightarrow (\beta, e^{i\phi}) \rightarrow (\beta', e^{i\phi'}) \rightarrow (\beta', \rho'), \\ D_5 &: (\beta, \rho) \rightarrow (\beta, e^{i\phi}) \rightarrow (e^{i\phi'}\beta', -e^{-i\phi'}) \dashrightarrow (\beta', e^{i\phi'}) \rightarrow (\beta', \rho'), \\ D_6 &: (\beta, \rho) \rightarrow (\beta, e^{i\phi}) \dashrightarrow (e^{i\phi}\beta, -e^{-i\phi}) \rightarrow (\beta', \rho'), \\ D_7 &: (\beta, \rho) \rightarrow (\beta, e^{i\phi}) \dashrightarrow (e^{i\phi}\beta, -e^{-i\phi}) \rightarrow (\beta', e^{i\phi'}) \rightarrow (\beta', \rho'), \\ D_8 &: (\beta, \rho) \rightarrow (\beta, e^{i\phi}) \dashrightarrow (e^{i\phi}\beta, -e^{-i\phi}) \rightarrow (e^{i\phi'}\beta', -e^{-i\phi'}) \dashrightarrow (\beta', e^{i\phi'}) \rightarrow (\beta', \rho'), \end{aligned} \quad (7)$$

here \rightarrow indicates the distance between two nodes using D in (6), and \dashrightarrow represents a path of zero length because of the third equivalence relations \sim_3 . The angles ϕ, ϕ' lie in $[\pi/3, 2\pi/3]$. Notice all the involved points other than (β, ρ) and (β', ρ') are in E . Figure 6 illustrates these paths as a diagram. Figure 7 illustrates the path in the lattice space \mathcal{L} showing the examples of D in green, D_3 from (7) in blue, and D_8 from (7) in red.

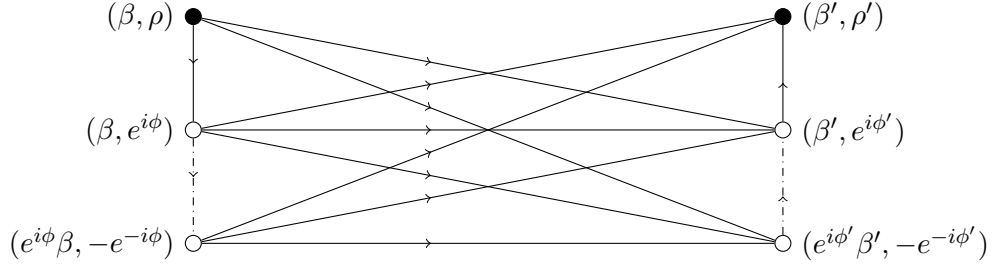


Figure 6: [Paths through E] This is an illustration of the 8 types of paths, $D_1 - D_8$ connecting (β, ρ) and (β', ρ') via points in $E = \{(\beta, \rho) \mid \beta \in \mathcal{K}, |\rho| = 1, \rho \in \mathcal{P}\}$. Notice all four points other than (β, ρ) and (β', ρ') are in E . The solid line represents the path length computed by D , while the dash line represents the third equivalence relation \sim_3 (no length added).

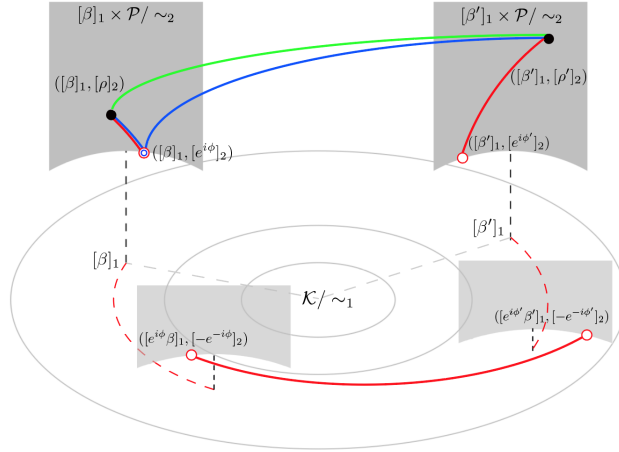


Figure 7: The lattice space \mathcal{L} is a product space $\mathcal{K}/\sim_1 \times \mathcal{P}/\sim_2$ modulo the points through E . The distance $d_{\mathcal{L}}((\beta, \rho), (\beta', \rho'))$ is the minimal lengths of the paths. Here the green line shows D in (6), the blue line is D_3 , and the red is D_8 in (7). Dash lines represent the third equivalence relations (no length).

Combining all these distance, **the metric** $d_{\mathcal{L}}$ between any two lattices $\Lambda(\beta, \rho)$ and $\Lambda(\beta', \rho') \in \mathcal{L}$ is defined as

$$d_{\mathcal{L}}((\beta, \rho), (\beta', \rho')) = \min\{D, \min_{\phi, \phi' \in [\pi/3, 2\pi/3]} D_j(\phi, \phi'), j = 1, \dots, 8\}, \quad (8)$$

here D is from (6), and $\{D_j(\phi, \phi')\}_{j=1}^8$ are from (7). For completeness, we present a pseudo-code for computing $d_{\mathcal{L}}$ in Appendix B. This metric $d_{\mathcal{L}}$ is the minimum among all the paths in $\mathcal{K}/\sim_1 \times \mathcal{P}/\sim_2$ connecting any two points (β, ρ) and (β', ρ') , thus $d_{\mathcal{L}}$ is a pseudometric on \mathcal{L} . In fact, $d_{\mathcal{L}}((\beta, \rho), (\beta', \rho')) = 0$ if and only if $[\beta, \rho] = [\beta', \rho']$, hence $d_{\mathcal{L}}$ becomes a metric on \mathcal{L} .

Remark 4.2. Notice that $d_{\mathcal{L}}$ is invariant under translation. It takes inputs from the lattice space \mathcal{L} , where only translational lattices are concerned. The visual difference between a lattice and its translated copy can be regarded as a consequence of the boundedness of the image domain, thus it is not intrinsic to the patterns.

4.1 Visual validation of the lattice space \mathcal{L} and metric $d_{\mathcal{L}}$

For the purpose of comparison, one may define the following 4-tuple from the classical definition 2.1 of lattice. For any minimal lattice basis (b_1, b_2) ,

$$(|b_1|, |b_2|, \theta, \psi) := (|b_1|, |b_2|, \text{Arg } b_1, \cos^{-1}(\frac{\text{Re}(b_1 \bar{b}_2)}{|b_1||b_2|})), \quad (9)$$

where θ taking values from $(-\pi/2, \pi/2]$ is the angle of b_1 to the positive real axis, and $\psi \in (0, \pi]$ is the angle between b_1 and b_2 . The differences in these parameters also reflect the visual differences in the lattice patterns.

Figure 8 and its table show effects of using the setting of (b_1, b_2) . Comparing a pair of very similar lattices in (a) $\Lambda_A = \Lambda(12, 12.5, 10^\circ, 90^\circ)$, and (b) $\Lambda_B = \Lambda(12, 12.5, -80^\circ, 90^\circ)$ expressed using the 4-tuples in (9), (9) gives a large relative difference for θ , 900%, while $d_{\mathcal{L}} = 0.0816$ gives a small value. When $|b_1| \approx |b_2|$, minor numerical errors trigger large relative errors in θ -component due to the equivalence relations. The lattices (a) Λ_A , (c) Λ_C , and (d) Λ_D , are more distinguishable, yet the differences in the second and third rows of the table fail to reflect this. $d_{\mathcal{L}}$ is more stable and consistent in representing the similarity and differences.

Figure 9 presents more examples of lattice patterns and their pairwise distances. There are five different lattices patterns shown in (a)-(e). Comparing lattices Λ_A to Λ_B or Λ_C , visually lattice Λ_C seems more different from Λ_A than Λ_B . The corresponding distances $d_{\mathcal{L}}(\Lambda_A, \Lambda_C) = 0.7083 > d_{\mathcal{L}}(\Lambda_A, \Lambda_B) = 0.5493$ are consistent with this observation. Among the lattices, visually Λ_A and Λ_D seems the most similar and $d_{\mathcal{L}}(\Lambda_A, \Lambda_D) = 0.0203$ is the smallest. The differences between lattice Λ_B and Λ_C , and the differences between lattice Λ_D and Λ_E , seems similar, and this is well represented by the distance $d_{\mathcal{L}}(\Lambda_B, \Lambda_C) = 0.4472$ and $d_{\mathcal{L}}(\Lambda_D, \Lambda_E) = 0.4472$ being close. Also the differences between Λ_B and Λ_D , and the differences between lattice Λ_C and Λ_E , are also similar $d_{\mathcal{L}}(\Lambda_B, \Lambda_D) = 0.5293$ and $d_{\mathcal{L}}(\Lambda_C, \Lambda_E) = 0.5293$.

5 New Lattice Identification and Separation Algorithm (LISA)

In this section, we propose an efficient algorithm to separate each lattice pattern from a super-lattice in practice. First, we present the variational formulation for lattice identification and separation. Then we introduce our algorithm which does not require any prior knowledge of the number lattice mixture.

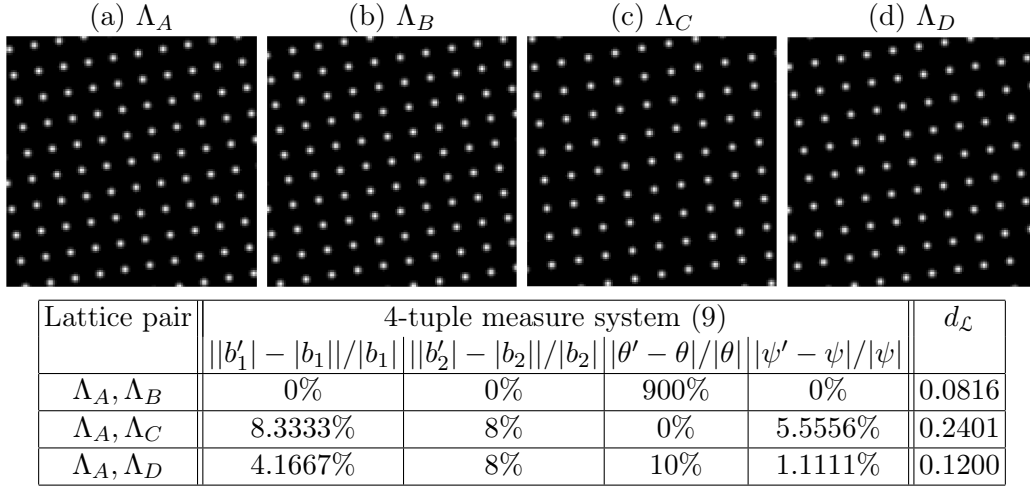


Figure 8: [Metric Comparison] Lattice (a) $\Lambda_A = \Lambda(11.8177 + 2.0838i, -2.1706 + 12.3101i)$ and (b) $\Lambda_B = \Lambda(2.0838 - 11.8177i, 12.3101 + 2.1706i)$ are visually similar. 4-tuple measure shows instability in the values, while $d_{\mathcal{L}}$ give a small value. The lattices (a), (c) $\Lambda_C = \Lambda(-1.1766 + 13.4486i, -2.0838 + 11.8177i)$ and (d) are more distinguishable. While 4-tuple measure doesn't reflect this consistently comparing the second and third row of the Table, $d_{\mathcal{L}}$ is more stable and consistent in representing the similarity and differences.

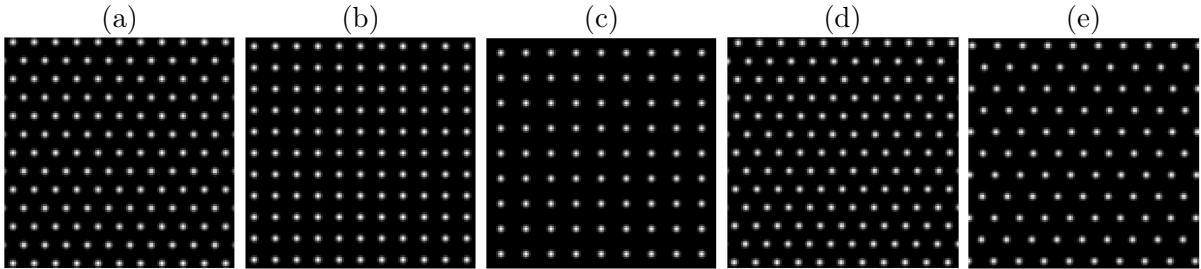


Figure 9: [Visual effects of $d_{\mathcal{L}}$] Five different lattices: (a) $\Lambda_A = \Lambda\langle 11, e^{i\pi/3} \rangle$ (b) $\Lambda_B = \Lambda\langle 11, e^{i\pi/2} \rangle$ (c) $\Lambda_C = \Lambda\langle 13, e^{i\pi/2} \rangle$ (d) $\Lambda_D = \Lambda\langle 11, e^{i61\pi/180} \rangle$ (e) $\Lambda_E = \Lambda\langle 13, e^{i61\pi/180} \rangle$. Pairwise distances: $d_{\mathcal{L}}(\Lambda_A, \Lambda_B) = 0.5493$, $d_{\mathcal{L}}(\Lambda_A, \Lambda_C) = 0.7083$, $d_{\mathcal{L}}(\Lambda_A, \Lambda_D) = 0.0203$, $d_{\mathcal{L}}(\Lambda_A, \Lambda_E) = 0.4477$, $d_{\mathcal{L}}(\Lambda_B, \Lambda_C) = 0.4472$, $d_{\mathcal{L}}(\Lambda_B, \Lambda_D) = 0.5293$, $d_{\mathcal{L}}(\Lambda_B, \Lambda_E) = 0.6929$, $d_{\mathcal{L}}(\Lambda_C, \Lambda_D) = 0.6929$, $d_{\mathcal{L}}(\Lambda_C, \Lambda_E) = 0.5293$, $d_{\mathcal{L}}(\Lambda_D, \Lambda_E) = 0.4472$. These values correspond well with the visual perception of the lattice differences.

5.1 Variational Model for Lattice Separation

For a given image with mixture of lattices $U : \Omega \subseteq \mathbb{R}^2 \rightarrow [0, 1]$ as in (1), we identify the underlying lattice patterns by minimizing the following energy:

$$\min_{K \in \mathbb{N}, \Lambda_j \in \mathcal{L}, \mu_j \in \mathbb{C}} \int_{\Omega} |U - \max_{j=1, \dots, K} \mathcal{T}_{\mu_j} \Lambda_j| dx dy + hK, \quad (10)$$

where $dx dy$ is the Lebesgue measure on \mathbb{R}^2 , and $h > 0$ is a penalty coefficient. To avoid identifying multiple sub-lattices to approximate a single denser lattice, we suppress the number of different lattice pattern while fitting the mixture to the given image. See more discussion on sub-lattice in Appendix A.

For a fixed K , this energy is balancing two competing terms. Using $|a-b| = a+b-2\min(a, b)$ for any $a, b \in \mathbb{R}$, the minimization (10) becomes:

$$\min_{\Lambda_j \in \mathcal{L}, \mu_j \in \mathbb{C}} \left\{ \int_{\Omega} U - \min(U, \max_{j=1, \dots, K} \mathcal{T}_{\mu_j} \Lambda_j) dx dy + \int_{\Omega} \sum_{j=1}^K \mathcal{T}_{\mu_j} \Lambda_j - \min(U, \max_{j=1, \dots, K} \mathcal{T}_{\mu_j} \Lambda_j) dx dy \right\}. \quad (11)$$

These integrals are equivalent to counting particles: if U and $\mathcal{T}_{\mu_j} \Lambda_j$, $j = 1, \dots, K$ denote the sets of particles they contain respectively, then we have the following correspondences:

$$\begin{aligned} \int_{\Omega} U - \min(U, \max_{j=1, \dots, K} \mathcal{T}_{\mu_j} \Lambda_j) dx dy &\iff U - U \cap \bigcup_{j=1}^K \mathcal{T}_{\mu_j} \Lambda_j, \\ \int_{\Omega} \max_{j=1, \dots, K} \mathcal{T}_{\mu_j} \Lambda_j - \min(U, \max_{j=1, \dots, K} \mathcal{T}_{\mu_j} \Lambda_j) dx dy &\iff \bigcup_{j=1}^K \mathcal{T}_{\mu_j} \Lambda_j - U \cap \bigcup_{j=1}^K \mathcal{T}_{\mu_j} \Lambda_j. \end{aligned}$$

The sets on the right hand sides can be further expressed as

$$\bigcap_{j=1}^K (U \cap (\mathcal{T}_{\mu_j} \Lambda_j)^c), \text{ and } \bigcup_{j=1}^K (\mathcal{T}_{\mu_j} \Lambda_j \cap U^c).$$

The problem (11) is thus equivalent to:

$$\min_{\Lambda_j \in \mathcal{L}, \mu_j \in \mathbb{C}} \left\{ \underbrace{\int_{\Omega} U - \max_{j=1, \dots, K} (\min(U, \mathcal{T}_{\mu_j} \Lambda_j)) dx dy}_{\text{under-fitting}} + \underbrace{\int_{\Omega} \max_{j=1, \dots, K} (\mathcal{T}_{\mu_j} \Lambda_j - \min(U, \mathcal{T}_{\mu_j} \Lambda_j)) dx dy}_{\text{over-fitting}} \right\}. \quad (12)$$

The first term in the objective function is to measure the remaining intensities of U after points being extracted by K lattices, i.e., the under-fitting. The second term evaluates the total excessive intensities of these K lattices, i.e., the over-fitting. As K increases, the under-fitting decreases. If we control the over-fitting to be 0, i.e., every lattice candidate has no extra lattice points, then by adding more layers, (11) reaches the minimum. Therefore, we solve (10) using a greedy strategy, which leads to LISA.

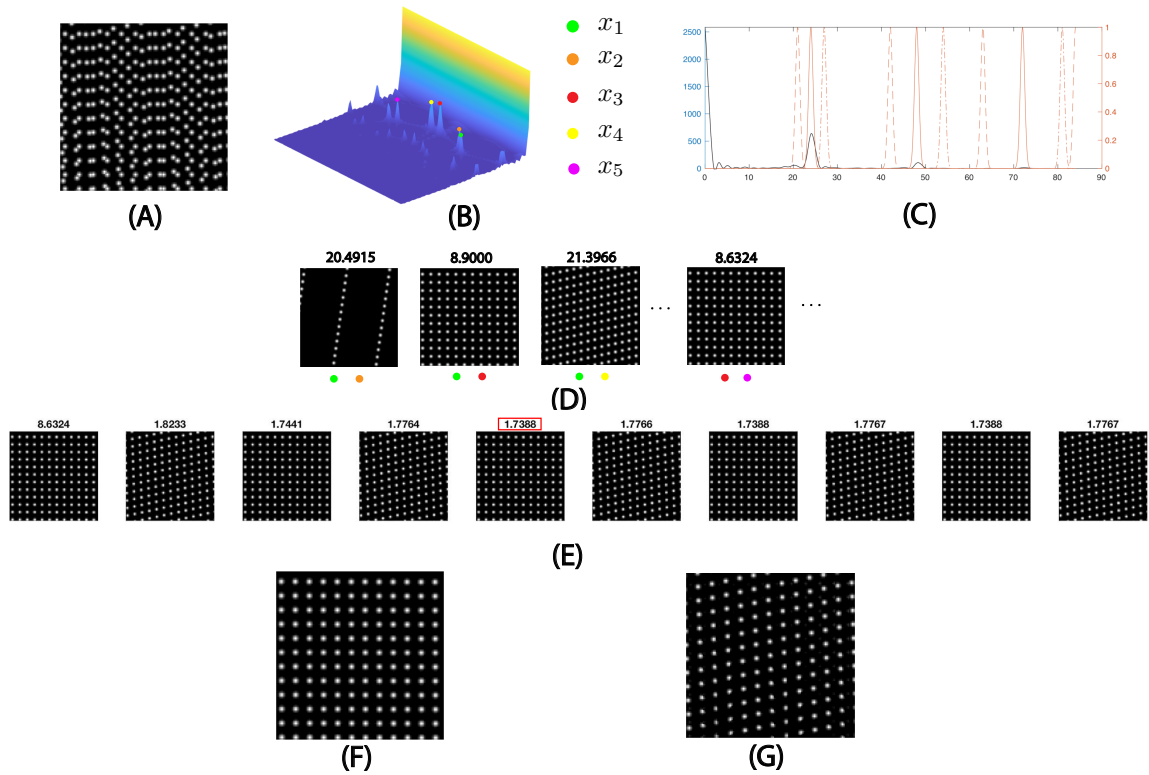


Figure 10: [Steps of LISA] (A) An image processed by \mathcal{F} (13). **Step1:** (B) the spectrum surface via polar coordinate, and the high responses x_1, \dots, x_5 above a threshold J . (C) peak location refinement via repeating Gaussian impulses. **Step 2:** (D) generates lattice candidates $\mathcal{T}_{\mu_{k,l}} \Lambda_{(k,l)}$, $k, l = 1, 2, \dots, 5, k \neq l$ for each pair of high peaks, and the energy (14) is computed for each candidate. Pick (x_3, x_5) to be the optimal $\mathcal{T}_{\mu_1} \Lambda_1$, for it has the lowest energy. **Step 3** (optional correction step): (E) Among $\mathcal{T}_{\mu_1} \Lambda_1^{(i)}$, $i = 1$ to K ($K = 10$) $\mathcal{T}_1 \Lambda_{\mu_1}^{(5)}$ has the lowest score, hence replaces $\mathcal{T}_{\mu_1} \Lambda_1$. **Step 4:** (F) The optimal lattice $\mathcal{T}_{\mu_1} \Lambda_1$ for this iteration. (G) The remainder image. The error is above the accuracy criteria $0.0710 > 0.01$, goes to next iteration.

Lattice Identification and Separation Algorithm (LISA)

Inputs:

1. U : given gray scale image with particles;
2. J : a parameter to control the number of lattice candidates;
3. (*Optional*) K : number of iteration for the optional step 3.

Let $j = 1$. While TRUE:

Step 1. Compute Fourier transform of U on polar coordinate. Collect the local maximum of spectrum surface of U , $C_j = \{x_1, x_2, \dots, x_M\}$ within J connected components.

Step 2. For every pair $(x_k, x_l) \in C_j$, $k \neq l$, construct a lattice pattern and compute the translation $\mu_{k,l}$ to get $\mathcal{T}_{\mu_{k,l}}\Lambda_{(k,l)}$. Take $\mathcal{T}_{\mu_j}\Lambda_j = \arg \min_{k,l=1,\dots,M;k \neq l} \mathcal{E}(\mathcal{T}_{\mu_{k,l}}\Lambda_{(k,l)})$ as in (14).

Step 3. (*Optional*) correction of $\mathcal{T}_{\mu_j}\Lambda_j$ using K iteration.

Step 4. For the identified optimal $\mathcal{T}_{\mu_j}\Lambda_j$, if $\text{mean}(U - \mathcal{T}_{\mu_j}\Lambda_j) < 0.01$, terminate the algorithm. Otherwise, set $U = \mathcal{F}(U - \mathcal{T}_{\mu_j}\Lambda_j)$, $j = j + 1$ and repeat.

Table 1: Lattice Identification and Separation Algorithm

5.2 Lattice Identification and Separation Algorithm (LISA)

The outline of the algorithm is presented in Table 1 and a demonstration of the workflow is in Figure 10.

In real applications, there are inhomogeneities in the particle sizes, shapes, and intensities, which complicates the identification. After background denoising (e.g., Otsu’s method [48]) if necessary, we process the image by replacing each local maximum in the image with a uniform size Gaussian PSF G_σ . We denote this processing as an operator \mathcal{F} :

$$\mathcal{F}(U) = G_\sigma * \delta(|\nabla U|). \quad (13)$$

For low or medium resolution, we apply the Gaussian approximation method to calibrate the peak locations as necessary (also see [45, 59, 46]). Let $U(x, y)$ be a discrete local maxima, i.e., $U(x, y) \geq U(x', y')$, for $x' = x \pm 1$ and $y' = y \pm 1$. The approximated coordinate for the real local maxima becomes:

$$\hat{x} = x - \frac{\log(U(x+1, y)) - \log(U(x-1, y))}{2(\log(U(x+1, y)) + \log(U(x-1, y)) - 2\log(U(x, y)))},$$

$$\hat{y} = y - \frac{\log(U(x, y+1)) - \log(U(x, y-1))}{2(\log(U(x, y+1)) + \log(U(x, y-1)) - 2\log(U(x, y)))}.$$

In Step 1, we compute the Radon transform by a B-spline convolution-based Radon transform proposed by Horbelt et al. [32]. The result is a 1D signal for each projecting angle, upon which we apply the standard 1D FFT. The collection of these 1D spectra form the 2D Fourier transform of the image on the polar coordinate (see Theorem 2.3), see Figure 10(b). For computational efficiency, we focus on peaks with sufficient heights, e.g. x_1, \dots, x_5 . This height threshold is picked such that, above it, there are J connected components of the power spectrum, i.e., $J = 5$ in Figure 10(b). To achieve sub-pixel precision, the distance of a peak response to the origin is adjusted by perturbation along the radial direction. Figure 10(c) demonstrates

this process: consider trains of Gaussian impulses placed periodically along the radial direction (periodicities perturbed around the peak distance to the origin), and choose the one with the most overlap with the signal to be the adjusted distance.

In Step 2, each pair of local maxima on the spectrum surface corresponds to a lattice candidate in the image domain. Figure 10(d) shows 4 examples of such combinations. Fourier transform of a lattice $\Lambda(b_1, b_2)$ in the image domain is a lattice in the frequency domain, called its reciprocal lattice $\Lambda(\omega_1, \omega_2)$. The formula transferring the basis (ω_1, ω_2) in frequency domain to the basis (b_1, b_2) in image domain is:

$$\begin{cases} b_1 = (\omega_2 \times [0, 0, 1]^T) / (|\omega_1 \times \omega_2 \cdot [0, 0, 1]^T|) \\ b_2 = ([0, 0, 1]^T \times \omega_1) / (|\omega_1 \times \omega_2 \cdot [0, 0, 1]^T|) \end{cases} .$$

The translation for each candidate, Figure 10(e), is then identified by the maximum of the cross-correlation function between the candidate and the original image. To evaluate the lattice candidates, we use the following energy:

$$\mathcal{E}(\mathcal{T}_\mu \Lambda) := \underbrace{\|\mathcal{F}(U - \mathcal{T}_\mu \Lambda) \odot \mathcal{F}(U)\|_2}_{\text{under-fitting}} + \gamma \underbrace{\left| \frac{\#\mathcal{T}_\mu \Lambda}{\#\mathcal{F}(\mathcal{T}_\mu \Lambda \odot U) + \varepsilon} - 1 \right|}_{\text{over-fitting}}, \quad \Lambda \in \mathcal{L}, \mu \in \mathbb{C}. \quad (14)$$

The optimal candidate has minimal energy. In (14), U denotes the original image, $\#\cdot$ represents counting the number of particles, and \odot is element-wise multiplication of matrices. The difference from the subtraction is truncated to non-negative parts. $\gamma > 0$ is a penalty coefficient (we set $\gamma = 10$), and $\varepsilon > 0$ is a small constant to avoid division by 0 (we set $\varepsilon = 1 \times 10^{-8}$).

Note that (14) is closely related to the energy (12). The first component in (14) measures the portion of particles not covered by the lattice candidate, i.e., the under-fitting. A smaller value means that more particles in the image lie on the lattice points of $\mathcal{T}_\mu \Lambda$. We normalize the remainder $U - \mathcal{T}_\mu \Lambda$ to make it comparable with $\mathcal{F}(U)$. The element-wise multiplication with $\mathcal{F}(U)$ prevents new points generated from incomplete particle extraction. The second term in (14) compares the ratio between the number of lattice points of the candidate, and the slots filled with particles from the image, i.e., the over-fitting.

Step 3, Figure 10(e), is similar to a sampling procedure with replacement. This step is optional, yet when the number of underlying lattices is large, it improve the accuracy of identification. As to be shown in subsection 5.3, superposing lattices complicates the power spectrum, hence early identification is affected the most. Incorrect early extraction further yields unstable identification for the remaining lattices. This optional step correct these aspects, and proceeds iteratively. We first set $t = 1$, and $\mathcal{T}_{\mu_j} \Lambda_j^{(1)} = \mathcal{T}_{\mu_j} \Lambda_j$. For $t = 1, \dots, K$, from the optimal lattice candidate $\mathcal{T}_{\mu_j} \Lambda_j^{(t)}$, compute the remainder $\mathcal{F}(U - \mathcal{T}_{\mu_j} \Lambda_j^{(t)})$ as in (13). Then iterate Step 1 and Step 2 on $\mathcal{F}(U - \mathcal{T}_{\mu_j} \Lambda_j^{(t)})$ to find the next optimal lattice $\mathcal{T}_{\mu_j} \Lambda_j^{(t+1)}$. This is the red boxed one in Figure 10(e). Update $\mathcal{T}_{\mu_j} \Lambda_j = \arg \min_{t=1, \dots, K} \mathcal{E}(\mathcal{T}_{\mu_j} \Lambda_j^{(t)})$. This optimal one is Figure 10(f).

In Step 4, the optimal candidate $\mathcal{T}_{\mu_j} \Lambda_j$ is subtracted from the original image, and the difference is truncated, only non-negative values remain. Figure 10(g) shows the remainder. We compute the average intensity of the residual $U - \mathcal{T}_{\mu_j} \Lambda_j$. Insufficient intensity terminates the algorithm (the threshold is set to be 0.01); otherwise, we preprocess the residual using \mathcal{F} replacing the original image and then repeat Step 1-4.

5.3 Analytical properties of LISA: Superlattice and Spectrum Surface

We describe the close relation between LISA and geometric features of the superlattice. Assuming no remainder term in the image representation (1), the Fourier transform of a superlattice image is:

$$\hat{U}(\xi) = \hat{G}_\sigma(\xi) \sum_{j=1}^N \frac{\Lambda_j^*(\xi)}{\det \Lambda_j} \exp(-i2\pi\xi \cdot \mu_j), \quad \xi \in \mathbb{R}^2, \quad (15)$$

where ξ represents the frequency coordinate, $\det \Lambda_j$ is the fundamental volume of $\Lambda_j = \Lambda\langle\beta_j, \rho_j\rangle$ computed by $\text{Im}(\overline{\beta_j}\beta_j\rho_j)$, and Λ_j^* denotes the reciprocal lattice impulse on the frequency domain corresponding to Λ_j , which is expressed in the lattice space by:

$$\Lambda_j^* = [\hat{\beta}_j, \hat{\rho}_j] := \left[\frac{\beta_j \exp(-i\pi/2)}{\det \Lambda_j}, \rho_j \right] \in \mathcal{L}.$$

Formula (15) implies that the Fourier transform of a superlattice image is a mixture of complex lattices modified by three factors: the centered Gaussian \hat{G}_σ , the fundamental volumes $\det \Lambda_j$, and the translations of the original lattices μ_j , $j = 1, 2, \dots, N$. Without these modulations, every lattice with two basis vectors in the image corresponds to two peaks on the power spectrum. Notice that $\Lambda_j^*(\xi) = 1$ if and only if $1/|\xi|$ is a period of Λ_j along the direction of ξ , $\forall \xi \in \mathbb{R}^2$ and $\forall j = 1, \dots, N$. Hence, lattices $\{\Lambda_j\}_{j=1}^N$ can be identified with correct combinations of the peaks.

Gaussian PSF and fundamental volumes of lattices complicate the problem. First, independent of the positions of the superlattice particles, a centered Gaussian \hat{G}_σ globally dampens the power spectrum. If $|\xi|$ is small, $\hat{G}_\sigma(\xi)$ has little influence on the power spectrum, and if $|\xi|$ is large, $\hat{G}_\sigma(\xi)$ decreases the value at ξ . Second, the radius of particles controls the rate of radial decay of the power spectrum surface. Large frequency components are preserved if the particles of the superlattice have a small radius, as the standard deviation σ is small. Third, fundamental volumes of the original lattices affect the power spectrum. The magnitudes of a pair of peaks on the spectrum surface associated with the lattices with smaller fundamental volumes are augmented, and those with larger fundamental volumes are decreased. This coincides with our experience that denser lattices are easier to be recognized. LISA tends to find lattices with smaller particles and smaller fundamental volumes.

Relative translations of the lattice layers have a more delicate influence on the power spectrum surface. Translation in spatial domain results in a phase change in the frequency domain, and it has no effect on the power spectrum if there is only one lattice. When multiple lattices are superposed, frequencies along the same direction will interact with each other. Suppose for some $1 < m \leq N$, $\Lambda_1^*(\xi) = \dots = \Lambda_m^*(\xi) = 1$ and $\Lambda_j^*(\xi) = 0$ for $j = m + 1, \dots, N$, then $\hat{U}(\xi)$ is a sum of m complex numbers, whose magnitude varies based on directions of μ_1, \dots, μ_m . An extreme case is that, if $\Lambda_1 = \Lambda_2$, $\mu_1 = -\mu_2 \neq 0$, and there exists an ξ such that $\Lambda_1^*(\xi) = 1$ and $\xi \cdot \mu_1 \neq 0$, then $|\hat{U}(\xi)| = 0$. See Figure 11 for an example. LISA detects potential lattices, even though the reciprocal lattices are incomplete and the reciprocal bases are not minimal. If any basis of the reciprocal lattice remains high response in the power spectrum, LISA will consider it as a candidate to be evaluated.

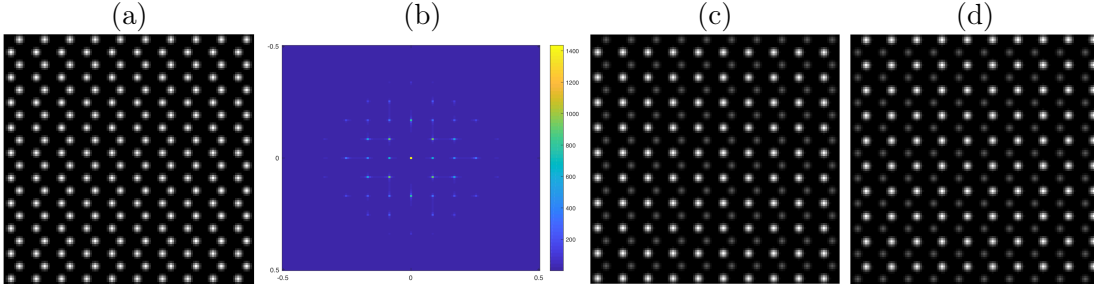


Figure 11: [Relative translation affects spectrum surface] Two lattices $\mathcal{T}_{4-3i}\Lambda\langle 12, i \rangle$ and $\mathcal{T}_{-4+3i}\Lambda\langle 12, i \rangle$ are superposed in (a). Due to the relative translations, there are missing peaks in the spectrum surface as shown in (b). From this incomplete reciprocal lattice, LISA recovers the lattices in (c) and (d).

5.4 Robustness of LISA against Gaussian Perturbation

Lattice distorted by Gaussian perturbation can model the atomic configuration in crystal-melt interface [13]. We modify (15) to consider such cases. For simple notations, only one unshifted lattice is assumed, and it is easy to extend to the general formula for multiple lattices with translations. Ignoring the remainders in (1), the image \tilde{U} of a lattice $\mathcal{T}_0\Lambda(b_1, b_2)$ with perturbed particles can be expressed as:

$$\tilde{U}(x, y) = \sum_{k_1, k_2 \in \mathbb{Z}} G_\sigma * \delta(k_1 b_1 + k_2 b_2 + \Delta x_{k_1, k_2} + i \Delta y_{k_1, k_2} - x - iy),$$

with $(\Delta x_{k_1, k_2}, \Delta y_{k_1, k_2}) \in \mathbb{R}^2$ denoting the perturbation on the particle parameterized by (k_1, k_2) in the lattice. The Fourier transform of \tilde{U} is

$$\hat{G}_\sigma(\xi) \sum_{k_1, k_2 \in \mathbb{Z}} \exp(-2\pi i \phi_{k_1, k_2}(\xi)),$$

where $\phi_{k_1, k_2}(\xi) = (\Delta x_{k_1, k_2} + i \Delta y_{k_1, k_2} + k_1 b_1 + k_2 b_2) \cdot \xi$. We assume that the perturbations are independent and identically distributed Gaussian vectors with uncorrelated coordinates, that is $(\Delta x_{k_1, k_2}, \Delta y_{k_1, k_2}) \sim \mathcal{N}(0, \Sigma)$ where $\Sigma = \begin{bmatrix} s^2 & 0 \\ 0 & s^2 \end{bmatrix}$, $s > 0$ constant, $\forall (k_1, k_2) \in \mathbb{Z}^2$. This implies that for any ξ in the frequency domain,

$$\phi_{k_1, k_2}(\xi) \sim \mathcal{N}((k_1 b_1 + k_2 b_2) \cdot \xi, s^2 |\xi|^2).$$

Some observations are immediate. First, for a single lattice, perturbations only alter the phases. Interactions among multiple lattices can still change the magnitude of the power spectrum as discussed in subsection 5.3. Second, $\mathbb{E}[\phi_{k_1, k_2}(\xi)]$ depends on the angle between $k_1 b_1 + k_2 b_2$ and ξ . In particular, perturbations have a stronger effect on non-lattice points than lattice points. If ξ is reciprocal to the lattice point $k_1 b_1 + k_2 b_2$, then they are perpendicular, thus the average perturbation is 0. Finally, with fixed s , the standard deviation of $\phi_{k_1, k_2}(\xi)$ only depends on $|\xi|$. When $|\xi|$ is small, or equivalently when we are approximating relatively large periods, the Fourier transform of the perturbed lattice is almost the same as that of the unperturbed one. In

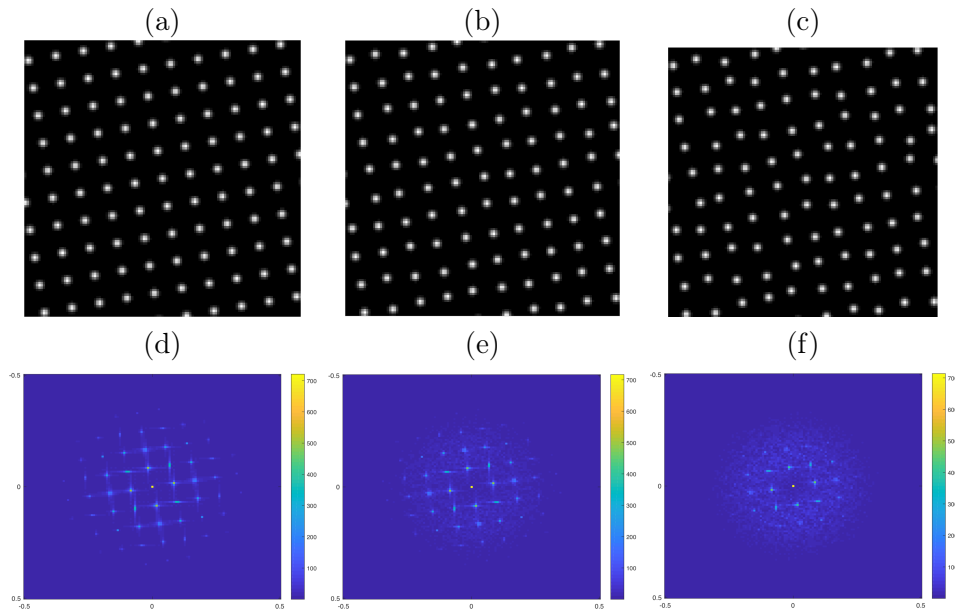


Figure 12: [LISA is robust against Gaussian perturbation] In the first column, a single lattice $\mathcal{T}_0\Lambda(12, e^{i\pi/18})$ is shown in (a) with its power spectrum surface in (d). A centered Gaussian perturbation is applied with standard deviation (b) $s = 0.5$ and (c) $s = 1$, and their power spectrums are displayed in (e) and (f) respectively. Notice that in the frequency domain, the reciprocal bases away from the origin are smeared by noises, but those near the origin remain high responses. The first lattices identified by LISA in (b) and (c) are robust against the perturbation, and their distances to (a) are 0.0046 and 0.0081 respectively.

Figure 12, lattice points are shifted by Gaussian perturbation with various standard deviations, and the low-frequency components maintain high responses. LISA is robust against Gaussian perturbation with bounded standard deviation, and the detection of medium-sized-lattices is effective. When the standard deviation is large, LISA identifies the correct lattices, yet the extraction may need other techniques, e.g., the nearest particles to the lattice candidate are identified.

6 Numerical Experiments of LISA

We present various numerical results. The radius of each particle is around $2.5 \sim 3$ pixels, and we choose 2.7, for visualization. The performance of LISA is evaluated both visually and numerically by computing the distances between the identified and the real patterns in the lattice space. For the choice of parameters, we fix $J = 6$ and $K = 10$.

Figure 13 shows a typical example of LISA. The given image is a superlattice composed of three distinguishable lattices. LISA successfully extracts all the underlying lattices, one after another. For better comparison, results (b)–(d) display each identified lattice (bright white) overlaid on a dimmer original image in (a). For each layer, the identified lattice and true lattice shows a small difference.

Figure 14 shows a more complicated mixture where the given image (a) seems almost ran-

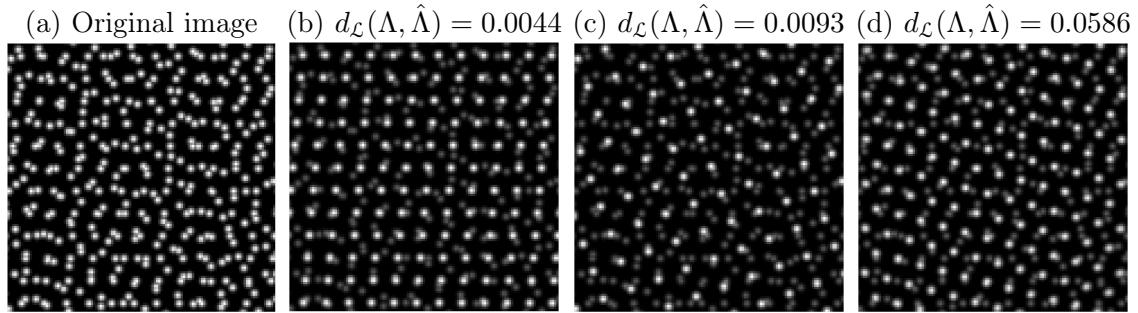


Figure 13: [Typical example of LISA] Identification of three lattices in (a). (b) is the extracted pattern for $\mathcal{T}_{2-4i}\Lambda\langle-9.9927 + 0.0315i, 1.0014e^{i17\pi/36}\rangle$, (c) is the extracted pattern for $\mathcal{T}_{-7-4i}\Lambda\langle-4.4820 + 12.1815i, i\rangle$. (d) is the extracted pattern for $\mathcal{T}_{1-5i}\Lambda\langle-4.9898 - 8.5389i, 1.0298e^{i7\pi/12}\rangle$. The metric value above the images shows the comparison with the true lattice and the recovery.

dom. The more layers of lattices there are, the more complicated the separation becomes. Randomly clustered particles, curve-like segments, and highly inhomogeneous texton regions present challenges. LISA identified five different lattice patterns from image (a), without any prior knowledge, and the recovered lattice patterns show high precision. The metric values below the images show the comparison with the true lattices, which are all less than 0.03. Also, notice that the identified lattice patterns (c) and (f) are very similar. Their lattice distance in the lattice space is 0.0340. LISA is able to distinguish small differences since in the power spectrum surface, periodic structures are more easily identified as strong responses.

The new lattice representation and the metric are independent to the translation of lattice pattern. Figure 15 presents the effect of LISA concerning the translation. There are two groups of lattices mixed in the given image (a), and each group has two lattices differing from each other only by translation μ . By cross-correlation function (in Step 2 of LISA), the underlying four lattices are extracted sequentially. We notice that even if particles are located close to each other, LISA is able to identify the underlying lattices. In Figure 16, a different set of translational lattices form a grand lattice pattern, whose lattice points are replaced by three dots, each of which belongs to a different lattice. Such configuration results in many L-shapes in the image [49]. This local ambiguity presents no confusion for LISA since it observes the image globally in the frequency domain. The sensitivity of LISA to the distance between particles is affected by the size of the particle of lattice candidates.

In practice, only a portion of the lattice patterns may be present. For example, Figure 17 (a) is a superlattice composed by a completely presented lattice (b) and a partially displayed lattice (c), where 50% of the particles are missing. The incompleteness modifies the power spectrum by convolving the reciprocal lattice of (c) with the Fourier transform of the lower triangular shape, resulting in weaker responses. Hence, LISA identifies the complete lattice (b) first, then reveals the incomplete lattice (c). Notice that LISA identifies the complete lattice pattern corresponding to (c), instead of the incomplete lattice image (c). This is shown in (e), where the identified pattern extends to the upper triangular region. A simple improvement of this visual presentation would be directly comparing the identified pattern with the original image, which is shown in (f). We also experiment in situations where 70% of the particles from

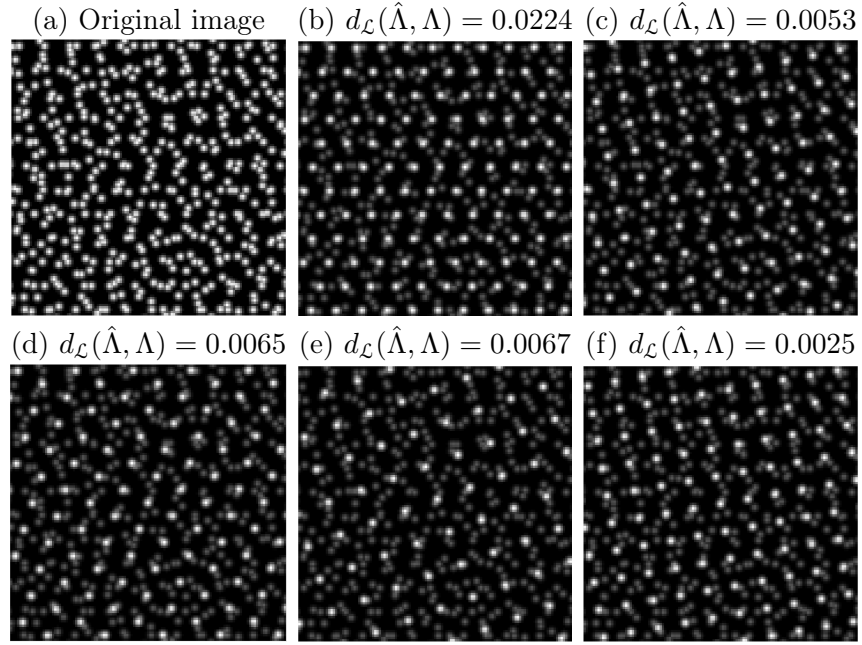


Figure 14: Identification of five lattices from the given image (a) using LISA. (b) The extracted pattern $\mathcal{T}_{2-5i}\Lambda\langle 11, e^{i7\pi/18} \rangle$, (c) $\mathcal{T}_{3+4i}\Lambda\langle 11.7378 + 2.4949i, i \rangle$, (d) $\mathcal{T}_0\Lambda\langle 3.7082 + 11.4127i, e^{4\pi/9} \rangle$, (e) $\mathcal{T}_{1-2i}\Lambda\langle 14.0954 + 5.1303i, i \rangle$, and (f) $\mathcal{T}_0\langle 11.8177 + 2.0838i, i \rangle$. LISA inspects the superlattice in frequency domain and avoids complexities in the image domain. Notice that all the metric value $d_{\mathcal{L}}(\hat{\Lambda}, \Lambda)$ comparing the recovered lattice with the true lattice are very small.

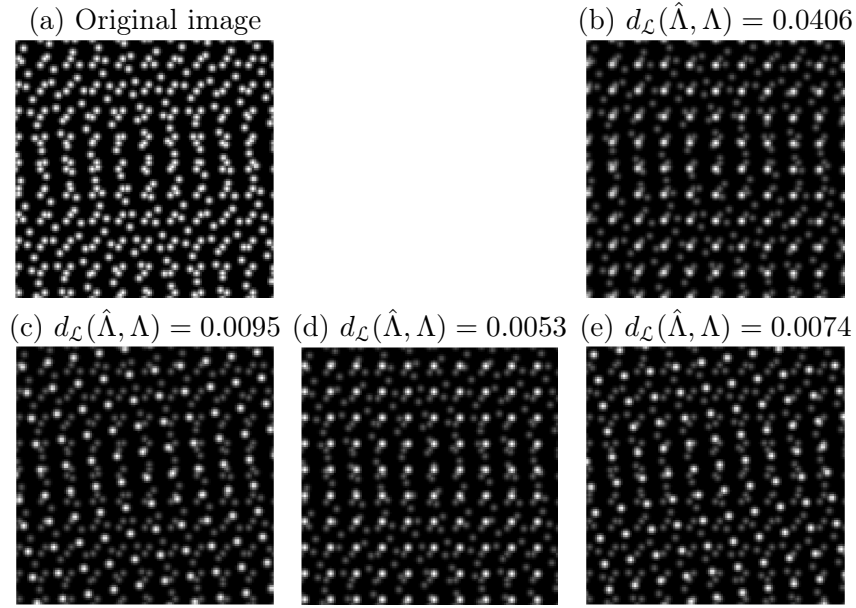


Figure 15: [Translation] Identification of four lattices in (a). Lattices identified in (b) $\mathcal{T}_0\Lambda\langle 12, i \rangle$ and (d) $\mathcal{T}_{2-3i}\Lambda\langle 12, i \rangle$ only differ by translation, so do those in (c) $\mathcal{T}_{1+i}\Lambda\langle 11.8177 + 2.0838i, i \rangle$ and (e) $\mathcal{T}_{2-5i}\Lambda\langle 11.8177 + 2.0838i, i \rangle$.

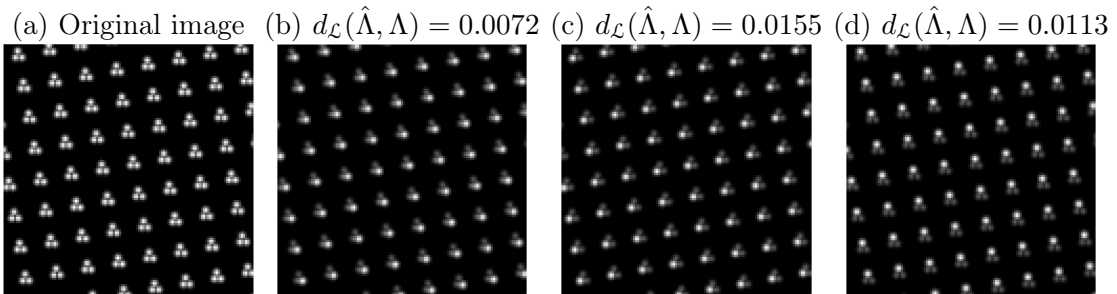


Figure 16: [Close translated particles] Identification of three lattices in (a). They are shifted from $\mathcal{T}_0\Lambda\langle 14.7721 + 2.6047i, i \rangle$ by (b) $4 - 2i$ (c) $1 - 2i$. (d) $2 - 5i$. These relative translations push particles close, and generate a lattice pattern whose lattice points are composed of three dots. LISA successfully distinguishes them with high precision as indicated by $d_{\mathcal{L}}(\hat{\Lambda}, \Lambda)$ values above each lattice.

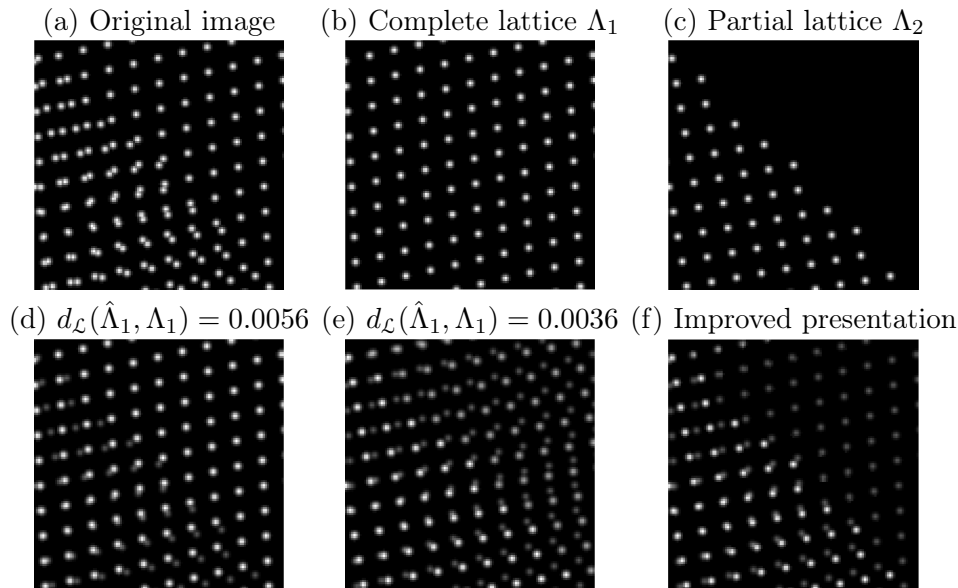


Figure 17: [Incomplete lattice] The superlattice in (a) is a mixture of (b) $\mathcal{T}_0\Lambda(11.6924 + 2.6994i, e^{i4\pi/9})$ and (c) $\mathcal{T}_{-3i}\Lambda(11.8177 + 2.0838i, i)$, which is incomplete. (d) and (e) are the identified patterns by LISA. By directly comparing (e) with (a), (f) improves the visual presentation.

one of the lattices are missing, and LISA recognizes the incomplete lattices successfully. An obvious upper bound for the number of missing particles is that the average intensity of the incomplete lattice must remain at least 0.01 by the terminating condition of LISA.

The evaluation method (14) proposed in section 5 considers the density restriction, i.e., the overfitting term. Figure 18 illustrates this importance. Image (a) is generated with two lattices presenting a region of moiré pattern in the center. Without the density restriction in (14), image (b) is identified while with the density restriction image (c) is the identified lattice. Comparing the lattice (b) and (c), shown in (d), (b) is dense and (c) is almost a sub-lattice of (b). Although (b) seems to have identified more points (according to (d)), comparing the lattice (b) with the given image (a), in fact, many points are not identified — shown in (e). In this case, lattice (c) was one of the underlying lattices. In the frequency domain, large-scale moiré patterns tend to produce strong responses on power spectrum surface. Lattice candidates associated with these high responses are excessively dense, and they partially coincide with the moiré patterns in the given image, which causes the next-level-identification unstable. Hence the density restriction in (14) makes LISA robust against possible moiré patterns.

Superposed lattices can present various attractive patterns, and the formation simply involves scaling and rotating. Hexagonal lattices, which share shape descriptors $\rho = \pm 1/2 + i\sqrt{3}/2$, produce the most variation. This is because, in the lattice space, their equivalent classes have the most elements, i.e., they are more symmetrical than the other lattices. In Figure 19, 4 hexagonal lattices with $\beta = 10, 12, 13$ and 15 are superposed, which displays a flake-like pattern. In Figure 20, a flower-like pattern is formed by 4 hexagonal lattices with identical scale descriptor norm $|\beta| = 11$ but different inclination angles: $53^\circ, -53^\circ, 143^\circ$ and -143° .

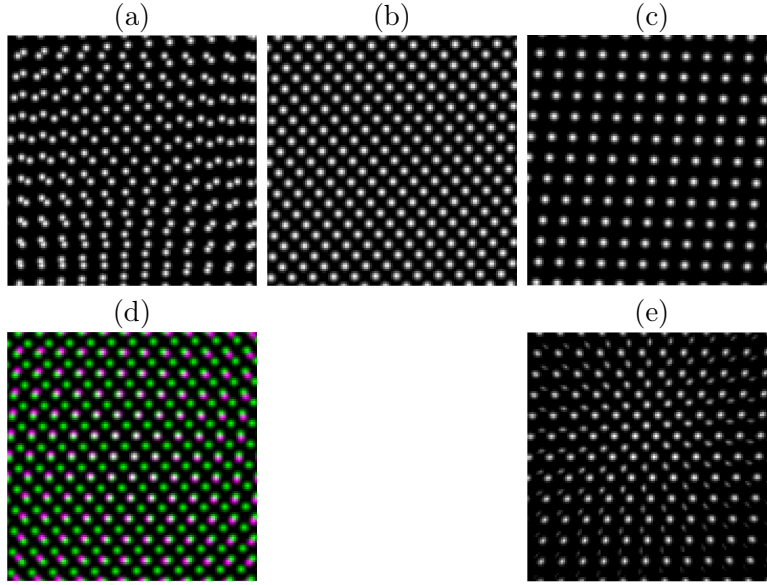


Figure 18: [Importance of density restriction] (a) Given image I generated by two lattices $\mathcal{T}_{2-10i}\Lambda\langle 10, e^{i17\pi/36} \rangle$, and $\mathcal{T}_{-3+5i}\Lambda\langle 9.9756 + 0.6976i, e^{i17\pi/36} \rangle$. If the score (14) does not have the second term, we obtain a dense lattice $\mathcal{T}\tilde{\Lambda}$ in (b). With the density restriction, we get $\mathcal{T}\hat{\Lambda}$ in (c) which is the correct lattice pattern. (d) compares patterns in (b) and (c) where white pixels are $\mathcal{T}\hat{\Lambda} \cap \mathcal{T}\tilde{\Lambda}$, the green are $\mathcal{T}\tilde{\Lambda} - \mathcal{T}\hat{\Lambda}$, and the red are $\mathcal{T}\hat{\Lambda} - \mathcal{T}\tilde{\Lambda}$. (e) displays $\min\{\mathcal{T}\tilde{\Lambda}, I\}$.

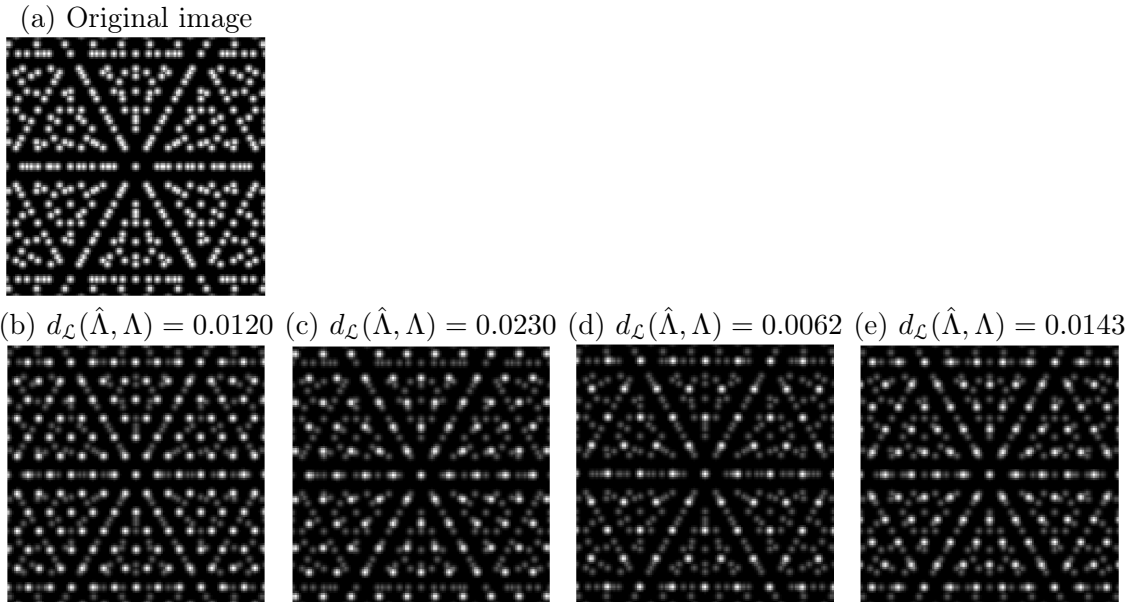


Figure 19: [Flake-like pattern generated by lattices] Identification of four lattices in the flake-like pattern in (a). The hexagonal lattices have scale descriptor β equal to (b) 10 (c) 13 (d) 15 and (e) 12.

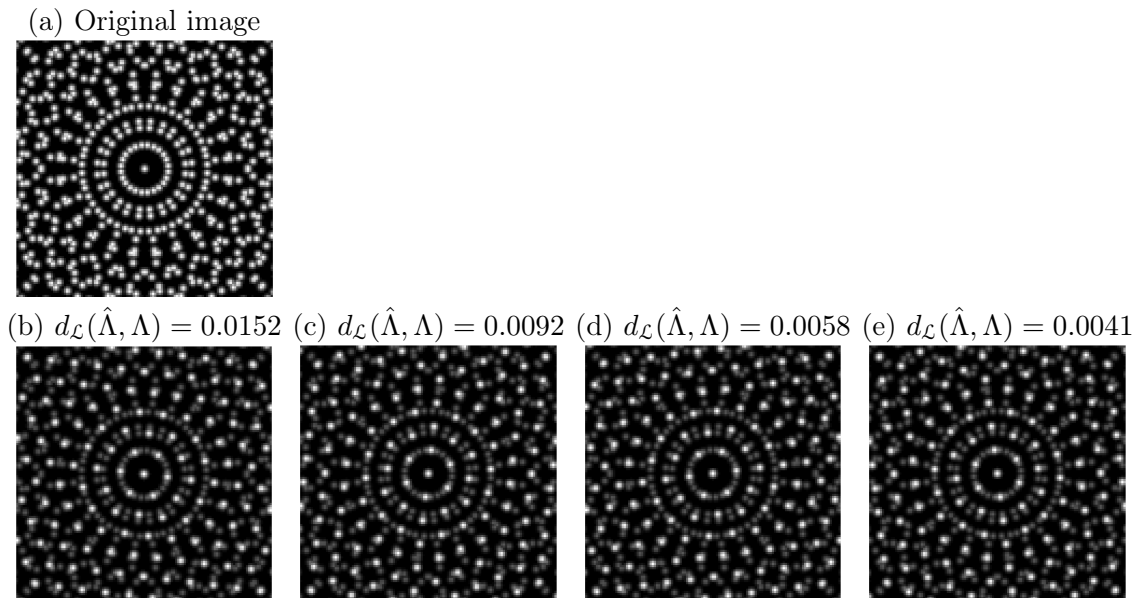


Figure 20: [Flower pattern generated by lattices] Identification of four lattices in the rotational pattern in (a). The hexagonal lattices with scale descriptors having common norm $|\beta| = 11$ have inclination angles equal to (b) 53° (c) 143° (d) -53° and (e) -143° .

Figure 21 (a) displays a portion of an image in [69], which is acquired by performing SAED on Na-exfoliated single-layer MoS_2 . As mentioned in the introduction, TMD monolayer has three layers of lattices. In the top-view, S-atoms on the top overlap with those in the bottom. LISA successfully identifies the visible lattices. Figure 21 (b) shows a part of a HREM image of single layer of MoSe_2 from [53]. Underlying lattices with bright lattice particles are identified and separated by LISA, yet the dimmer lattice particles fail to be recognized. This can be addressed by lowering the threshold obtained by Otsu’s method, image enhancing techniques, or sophisticated feature point detectors.

We also test LISA on an important class of images in material sciences focusing on the grain boundaries. Patches of regular lattices are identified using LISA, then by directly comparing with the preprocessed image, regions of homogeneous patterns are separated. Consequently, the grain boundary is revealed. Figure 22(a) shows a part of an image from [10], where a grain boundary is formed in the graphene grown by chemical vapor deposition (CVD). LISA detects two lattices as in (b) and (c). In (d), particles in (b) shared with the preprocessed image is colored green, those in (c) are red, and the white pixel indicates where (b) and (c) intersect. This example shows the potential applications of LISA besides superlattice separation.

Finally, we investigate the efficiency of LISA. We focus on three major factors contributing to the runtime of LISA: image size, number of connected components on the spectrum surface (J in Table 1), and the number of stabilizing iteration (K in Table 1). Fixing a superlattice consisting of two lattices $\mathcal{T}_0\Lambda\langle 12, i \rangle$ and $\mathcal{T}_0\Lambda\langle 11.2763 + 4.1042i, e^{i4\pi/9} \rangle$, the CPU times (in second) of LISA are plotted against each one of these factors when the other two are controlled. The results show that the complexity of LISA depends linearly on J and K , and quadratically on the image width. This is consistent with the analysis in [32], where the complexity of B-

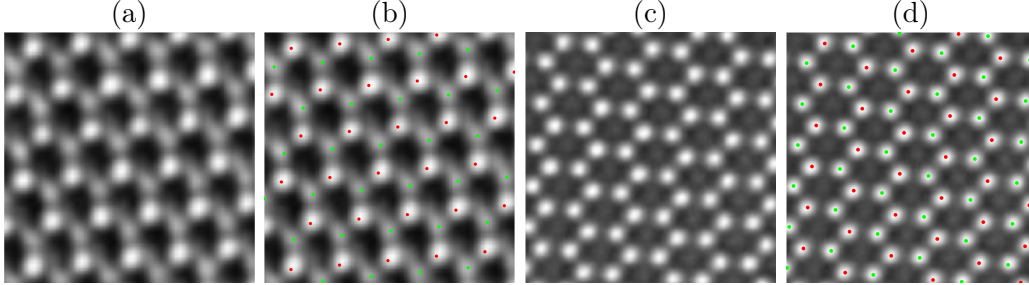


Figure 21: [LISA on real images] The underlying lattices in TMD monolayers (a) and (c) detected and separated by LISA are presented in (b) and (d) respectively, using different colors. (a) is cropped from [69] Figure 3 (c), and (c) is cropped from [53] Figure 1 (c).

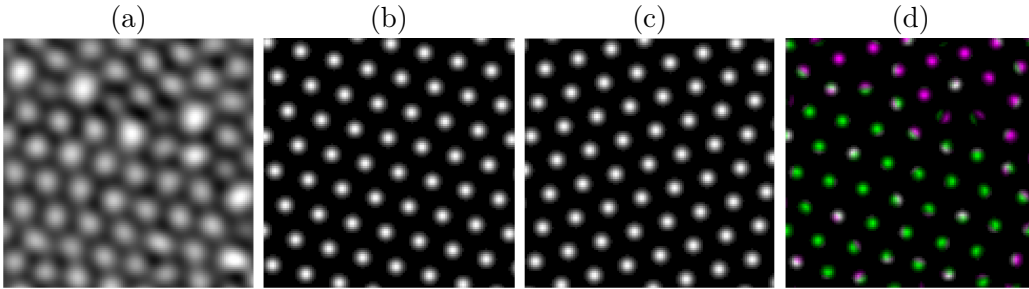


Figure 22: [LISA on grain boundary] A grain boundary in graphene formed by CVD is shown in (a). LISA detects the lattice in (b) $\mathcal{T}_{-1.3794+9.7510i}\langle -10.9881 - 12.1163i, -0.4579 + 0.8950i \rangle$ and in (c) $\mathcal{T}_{9.6287+9.5640i}\langle -15.7326 - 4.7420i, 0.4813 + 0.8800i \rangle$. (d) shows the homogeneous regions in different color, and the grain boundary is revealed. (a) is adjusted from [10] Figure 15 (a)

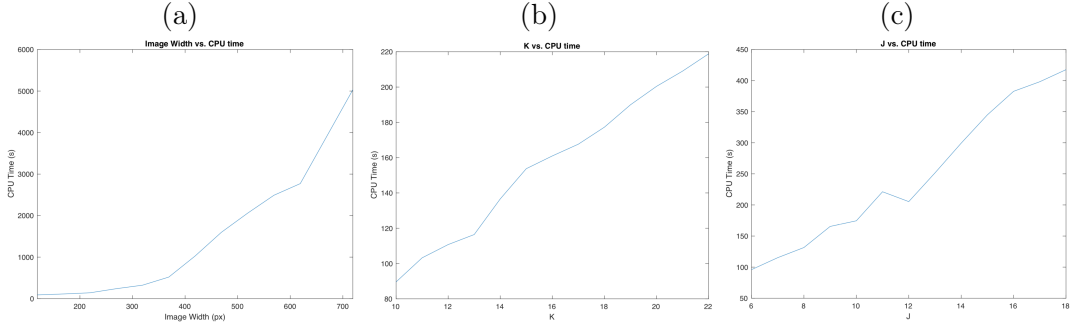


Figure 23: [CPU time of LISA] Fixing two lattices, the base image width is 119, $K = 10$, $J = 6$. Changing image size (a), the number of stabilizing iteration K (b) or the number of connected components J (c), while keeping the other two as in the base case, the CPU times (in sec) of LISA are plotted respectively.

spline convolution-based Radon transform is proportional to the image size, i.e., image width times image length.

7 Summary

This paper addresses two questions of lattice identification and separation in superlattices. The first one is: *What is a proper space where any two lattices can be compared quantitatively?* Starting from the positive minimal bases, we exploit the modular group theory and Poincaré metric to define a lattice space \mathcal{L} with a natural metric structure. This new definition provides rich geometrical intuition for the collection of lattices. Computation of the metric $d_{\mathcal{L}}$ yields compact and visually consistent information about differences between lattice patterns. Compatible with wallpaper group theory, \mathcal{L} provides finer classifications, which is more suitable for the purpose of measurement.

The second question is: *How to practically identify and separate lattices from a superlattice?* We introduce the algorithm LISA. Without prior knowledge of the lattices and number of layers of superposed lattices, LISA sequentially identifies and extracts lattice patterns until the remainder has insufficient intensity. We show the importance of density restriction when evaluating lattice candidates, which are indicated by pairs of high responses on the spectrum surface. This evaluation method renders LISA’s robustness against moiré patterns. An analytical framework is presented to consider the effects of relative translations and Gaussian perturbation. The metric space $(\mathcal{L}, d_{\mathcal{L}})$ allows more discussion about special families of lattices, and its geometrical properties are interesting to explore. LISA produces a series of regular lattice patterns, which can be extended to the separation of near-regular lattices, and identification of grain boundaries.

A Sub-lattices and Parent-lattices in Lattice Space

In section 3, we regard the collection of Möbius transforms as a group, and exploit its subgroup, the modular group Γ , to address the problems of basis representation. More generally, the group

of Möbius transforms has a monoid structure, i.e., inverse elements are not required compared with the group definition. In this section, we explore further the value of Möbius transforms by investigating one of its submonoids, $M_2(\mathbb{Z})$. We present the close relation between sub-lattices of a lattice and the monoid $M_2(\mathbb{Z})$. A one-to-one correspondence between sub-lattices and parent-lattices of a lattice is then proved to extend this relation to that between parent-lattices and $M_2(\mathbb{Z})$.

This section also has a practical significance. In section 5, when evaluating lattice candidates, the confusion caused by inhomogeneous texton regions and moiré effect is eliminated by attaching a density restriction in (14). The necessity of the density term is theoretically driven from the framework of this section.

A.1 Sub-lattices and Parent-lattices using Descriptors

The classical notions of sub- and parent-lattices can be paraphrased using descriptors β and ρ .

Definition A.1 (Sub-lattice). Let $\Lambda = \Lambda\langle\beta, \rho\rangle$ and $\Lambda' = \Lambda\langle\beta', \rho'\rangle$ be two lattices. We say that Λ' is a sub-lattice of Λ , if there exists $(k_1, k_2, k_3, k_4) \in \mathbb{Z}^4$ with $k_1k_4 - k_2k_3 > 0$ such that:

$$\begin{cases} \beta' = \beta(k_1 + k_2\rho) \\ \rho' = (k_3 + k_4\rho)/(k_1 + k_2\rho) \end{cases} .$$

And $\Lambda\langle\beta', \rho'\rangle$ is said to be a sub-lattice of $\Lambda\langle\beta, \rho\rangle$ induced by (k_1, k_2, k_3, k_4) .

This definition is derived from the equivalent expression:

$$\begin{cases} \beta' = k_1\beta + k_2\beta\rho \\ \beta'\rho' = k_3\beta + k_4\beta\rho \end{cases}$$

with $k_1k_4 - k_2k_3 > 0$, which says that the basis for a sub-lattice comes from a non-degenerate linear combination of the basis of the original lattice using integer coefficients. The transformations

$$z \mapsto \frac{k_3 + k_4z}{k_1 + k_2z}, \{k_i\}_{i=1}^4 \subset \mathbb{Z}, \text{ such that } k_1k_4 - k_2k_3 > 0, \text{ for any } z \in \mathcal{H}.$$

form a monoid with function composition, which is denoted by $M_2(\mathbb{Z})$. In the category of monoids, $\text{PSL}_2(\mathbb{Z}) \leq M_2(\mathbb{Z}) \leq \text{PGL}_2(\mathbb{Z})$, hence the discussion here is a generalization of section 3. Symmetrically, we define parent-lattices as follows:

Definition A.2 (Parent-lattice). Let $\Lambda = \Lambda\langle\beta, \rho\rangle$ and $\Lambda' = \Lambda\langle\beta', \rho'\rangle$ be two lattices. We say that Λ' is a parent-lattice of Λ , if there exists $(k_1, k_2, k_3, k_4) \in \mathbb{Z}^4$ with $v := 1/(k_1k_4 - k_2k_3) > 0$ such that:

$$\begin{cases} \beta' = v\beta(k_1 + k_2\rho) \\ \rho' = (k_3 + k_4\rho)/(k_1 + k_2\rho) \end{cases} .$$

Λ' is said to be a parent-lattice of Λ induced by (k_1, k_2, k_3, k_4) .

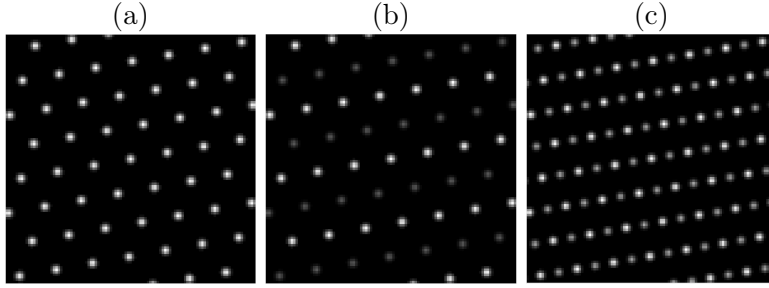


Figure 24: [One-to-one correspondence between sub- and parent-lattice] (a) is a lattice $\Lambda\langle\beta, \rho\rangle = \Lambda\langle 14.7721 + 2.6047i, e^{i\pi/3}\rangle$. $\Lambda\langle\beta, 2\rho + 1\rangle$ gives a sub-lattice in (b) and it corresponds to a parent-lattice $\Lambda\langle\beta/2, 2\rho + 1\rangle$.

This definition is equivalent to the normal notion of parent-lattice. Suppose Λ' is a parent-lattice of Λ in the normal sense, then there exist real numbers a, b, c, d with $u := ad - cb > 0$ such that:

$$\begin{cases} \beta' = a\beta + b\rho \\ \beta'\rho' = c\beta + d\rho \end{cases} \iff \begin{cases} \beta = d\beta'/u - b\rho'/u \\ \beta\rho = -c\beta'/u + a\rho'/u \end{cases} . \quad (16)$$

Since symmetrically Λ is a sub-lattice of Λ' , we have that $k_4 = d/u, k_2 = b/u, k_3 = c/u$ and $k_1 = a/u$ are actually integers. Therefore, (16) becomes:

$$\begin{cases} \beta' = \beta(k_1 + k_2\rho)u \\ \rho' = (k_3 + k_4\rho)/(k_1 + k_2\rho) \end{cases} .$$

But also notice that $k_1k_4 - k_2k_3 = (ad - cb)/u^2 = 1/u$, so we prove our claim. After checking the equivalence relations among descriptors, we have the following proposition,

Proposition A.3. *Given a lattice $\Lambda = \Lambda\langle\beta, \rho\rangle$, we have the following one-to-one correspondence:*

$$\{\text{Sub-lattices of } \Lambda\} \xleftrightarrow{\varphi} \{\text{Parent-lattices of } \Lambda\} \quad (17)$$

via φ well-defined as follows: if (k_1, k_2, k_3, k_4) determines a sub-lattice via (A.1), then they determine a parent-lattice via (A.2).

An example of this correspondence is in Figure 24. Once we find all the sub-lattices of a lattice, all its parent-lattices come for free. For a given lattice $\Lambda\langle\beta, \rho\rangle$, we only need to focus on finding $(k_1, k_2, k_3, k_4) \in \mathbb{Z}^4$ such that $(k_3 + k_4\rho)/(k_1 + k_2\rho)$ remains in \mathcal{P} .

A.2 $M_2(\mathbb{Z})$ -actions and Sub-lattices

As suggested above, we consider an element in $M_2(\mathbb{Z})$ whose image of \mathcal{P} has non-empty intersection with \mathcal{P} . It suffices to see its action on three distinct points. Generally, given a $\rho \in \mathcal{P}$, finding all such possible integer coefficients is hard and not fruitful. There are two most easily found families of sub-lattices:

1. Corresponding to $(k_1, k_2, k_3, k_4) = (n, 0, 0, 1)$, if $[\beta, \rho] \in \mathcal{L}$ with $|\rho| \geq n$, $n \in \mathbb{N}_{\geq 1}$, then for any $m \leq n$, $[m\beta, \rho/m]$ is a sub-lattice of $[\beta, \rho]$.
2. Corresponding to $(k_1, k_2, k_3, k_4) = (1, 0, 0, n)$, if $[\beta, \rho] \in \mathcal{L}$ with $|\operatorname{Re}(\rho)| \leq 1/(2n)$, $n \in \mathbb{N}_{\geq 1}$, then for any $m \leq n$, $[\beta, m\rho]$ is a sub-lattice of $[\beta, \rho]$.

In some special cases, it is also easy to find conditions for $(k_1, k_2, k_3, k_4) \in \mathbb{Z}^4$ such that there exists some $\rho \in \mathcal{P}$ who can be mapped to \mathcal{P} . For example, when $k_2 = 0$ (which forces $k_1 \neq 0$), we find $\infty \rightarrow \infty$, $0 \mapsto k_3/k_1$ and $\pm 1/2 \mapsto (\pm k_4/2 + k_3)/k_1$ by the $M_2(\mathbb{Z})$ -action determined by this (k_1, k_2, k_3, k_4) . In order to have non-empty intersection with \mathcal{P} , we must require:

$$\begin{aligned} \min\{(\pm k_4/2 + k_3)/k_1\} &\leq 1/2 \quad \text{or} \\ k_3^2 - k_4^2/4 < 0 \text{ and } \min\{(\pm k_4/2 + k_3)/k_1\} &\geq 1/2. \end{aligned}$$

By the correspondence in (17), these results also extend symmetrically to parent-lattices.

B Pseudo-code for computing $d_{\mathcal{L}}$

The definition of $d_{\mathcal{L}}$ (8) requires multiple comparisons. For paths passing through $E = \{(\beta, \rho) \mid \beta \in \mathcal{K}, |\rho| = 1, \rho \in \mathcal{P}\}$, minimizations are involved.

Inputs: two lattice bases (b_1, b_2) and $(b'_1, b'_2) \in \mathbb{C}^2$.

Step 1. Transfer to descriptors: $\beta \leftarrow b_1$, $\beta' \leftarrow b'_1$, $\rho \leftarrow b_2/b_1$, and $\rho' \leftarrow b'_2/b'_1$.

Step 2. Define two sub-routines:

$$\begin{aligned} D_{\mathcal{K}} : (x, y) \in \mathbb{C}^2 &\mapsto \sqrt{w(|x| - |y|)^2 + (1 - w)(\cos^{-1} \frac{\operatorname{Re}(x\bar{y})}{|x||y|})^2}, \quad (w = 0.05) \\ D_{\mathcal{P}} : (x, y) \in \mathbb{C}^2 &\mapsto 2 \ln \frac{|x - y| + |x - \bar{y}|}{2\sqrt{\operatorname{Im}(x)\operatorname{Im}(y)}}. \end{aligned}$$

Extend them to two new sub-routines by:

$$\begin{aligned} d_{\mathcal{K}} : (x, y) \in \mathbb{C}^2 &\mapsto \min\{D_{\mathcal{K}}(x, y), D_{\mathcal{K}}(-x, y)\}. \\ d_{\mathcal{P}} : (x, y) \in \mathbb{C}^2 &\mapsto \min\{D_{\mathcal{P}}(x, y), D_{\mathcal{P}}(x - 1, y), D_{\mathcal{P}}(x + 1, y)\}. \end{aligned}$$

Then define:

$$D : (x, y, z, w) \in \mathbb{C}^2 \mapsto \sqrt{d_{\mathcal{K}}(x, z)^2 + d_{\mathcal{P}}(y, w)^2}$$

Step 3. Fix an integer N .

For $j = 0, 1, \dots, N$:

For $k = 0, 1, \dots, N$:

$$\begin{aligned} D_{j,k} &\leftarrow d(\beta, \rho', \beta, \rho'); \\ D_{j,k} &\leftarrow \min\{D_{j,k}, d(\beta, \rho, \beta', e^{i(\pi/3+k\pi/3)}) + d(\beta', e^{i(\pi/3+k\pi/3)}, \beta', \rho')\}; \\ D_{j,k} &\leftarrow \min\{D_{j,k}, d(\beta, \rho, e^{i(\pi/3+k\pi/3)}\beta', -1/e^{i(\pi/3+k\pi/3)}) + d(\beta', e^{i(\pi/3+k\pi/3)}, \beta', \rho')\}; \\ D_{j,k} &\leftarrow \min\{D_{j,k}, d(\beta, \rho, \beta, e^{i(\pi/3+j\pi/3)}) + d(\beta, e^{i(\pi/3+j\pi/3)}, \beta', \rho')\}; \\ D_{j,k} &\leftarrow \min\{D_{j,k}, d(\beta, \rho, \beta, e^{i(\pi/3+j\pi/3)}) + d(\beta, e^{i(\pi/3+j\pi/3)}, \beta', e^{i(\pi/3+k\pi/3)}) + d(\beta', e^{i(\pi/3+k\pi/3)}, \beta', \rho')\}; \end{aligned}$$

$$\begin{aligned}
D_{j,k} &\leftarrow \min\{D_{j,k}, d(\beta, \rho, \beta, e^{i(\pi/3+j\pi/3)}) + d(\beta, e^{i(\pi/3+j\pi/3)}, e^{i(\pi/3+k\pi/3)}\beta', -1/e^{i(\pi/3+k\pi/3)}) + \\
&d(e^{i(\pi/3+k\pi/3)}\beta', -1/e^{i(\pi/3+k\pi/3)}, \beta', \rho')\}; \\
D_{j,k} &\leftarrow \min\{D_{j,k}, d(\beta, \rho, \beta, e^{i(\pi/3+j\pi/3)}) + d(e^{i(\pi/3+j\pi/3)}\beta, -1/e^{i(\pi/3+j\pi/3)}, \beta', \rho')\}; \\
D_{j,k} &\leftarrow \min\{D_{j,k}, d(\beta, \rho, \beta, e^{i(\pi/3+j\pi/3)}) + d(e^{i(\pi/3+j\pi/3)}\beta, -1/e^{i(\pi/3+j\pi/3)}, \beta', e^{i(\pi/3+j\pi/3)}) + \\
&d(\beta', e^{i(\pi/3+j\pi/3)}, \beta', \rho')\}; \\
D_{j,k} &\leftarrow \min\{D_{j,k}, d(\beta, \rho, \beta, e^{i(\pi/3+j\pi/3)}) + d(e^{i(\pi/3+j\pi/3)}\beta, -1/e^{i(\pi/3+j\pi/3)}, \dots \\
&e^{i(\pi/3+j\pi/3)}\beta', -1/e^{i(\pi/3+j\pi/3)}) + d(\beta', e^{i(\pi/3+j\pi/3)}, \beta', \rho')\};
\end{aligned}$$

End For

End For

$$d_{\mathcal{L}}((\beta, \rho), (\beta', \rho')) \leftarrow \min_{j,k} D_{j,k}.$$

References

- [1] G.B. Airy. On the diffraction of an object-glass with circular aperture. *Transactions of the Cambridge Philosophical Society*, 5:283, 1835.
- [2] M. Ajtai. The shortest vector problem in L2 is NP-hard for randomized reductions. In *Proceedings of the thirtieth annual ACM symposium on Theory of computing*, pages 10–19. ACM, 1998.
- [3] R.C. Alperin. Notes: $\mathrm{PSL}_2(\mathbb{Z}) = \mathbb{Z}_2 * \mathbb{Z}_3$. *Amer.Math.Monthly*, 100(4):385–386, 1993.
- [4] I. Amidror. *The Theory of the Moiré Phenomenon: Volume I: Periodic Layers*, volume 38. Springer Science & Business Media, 2009.
- [5] T.M. Apostol. *Modular functions and Dirichlet series in number theory*, (1990).
- [6] G.A. Bassett, J.W. Menter, and D.W. Pashley. Moiré patterns on electron micrographs, and their application to the study of dislocations in metals. *Proc. R. Soc. Lond. A*, 246(1246):345–368, 1958.
- [7] Benjamin Berkels, Andreas Rätz, Martin Rumpf, and Axel Voigt. Identification of grain boundary contours at atomic scale. In *International Conference on Scale Space and Variational Methods in Computer Vision*, pages 765–776. Springer, 2007.
- [8] Benjamin Berkels, Andreas Rätz, Martin Rumpf, and Axel Voigt. Extracting grain boundaries and macroscopic deformations from images on atomic scale. *Journal of Scientific Computing*, 35(1):1–23, 2008.
- [9] L. Bieberbach. Über die bewegungsgruppen der euklidischen räume. *Mathematische Annalen*, 70(3):297–336, 1911.
- [10] L.P. Biró and P. Lambin. Grain boundaries in graphene grown by chemical vapor deposition. *New Journal of Physics*, 15(3):035024, 2013.
- [11] C.M. Bishop. *Pattern Recognition and Machine Learning*. New York: Springer, 2006.
- [12] M. Boerdgen, B. Berkels, M. Rumpf, and D. Cremers. Convex relaxation for grain segmentation at atomic scale. In *VMV*, pages 179–186, 2010.

- [13] A. Bonissent and F.F Abraham. Application of perturbation theory to the crystal–melt interface. *The Journal of Chemical Physics*, 74(2):1306–1309, 1981.
- [14] Y.Y. Boykov and M.P. Jolly. Interactive graph cuts for optimal boundary & region segmentation of objects in ND images. In *Computer Vision, 2001. ICCV 2001. Proceedings. Eighth IEEE International Conference on*, volume 1, pages 105–112. IEEE, 2001.
- [15] R.N. Bracewell. Strip integration in radio astronomy. *Australian Journal of Physics*, 9(2):198–217, 1956.
- [16] D. Burago, Y. Burago, and S. Ivanov. *A course in metric geometry*, volume 33. American Mathematical Soc., 2001.
- [17] J.W.S. Cassels. *Rational quadratic forms*. Courier Dover Publications, 2008.
- [18] W. Choi, N. Choudhary, G.H. Han, J. Park, D. Akinwande, and Y.H. Lee. Recent development of two-dimensional transition metal dichalcogenides and their applications. *Materials Today*, 20(3):116–130, 2017.
- [19] W.P. Davey. Precision measurements of the lattice constants of twelve common metals. *Physical Review*, 25(6):753, 1925.
- [20] A. Eftekhari. Tungsten dichalcogenides (ws 2, wse 2, and wte 2): materials chemistry and applications. *Journal of Materials Chemistry A*, 5(35):18299–18325, 2017.
- [21] H.M. Farkas and I. Kra. Riemann surfaces. In *Riemann surfaces*, pages 9–31. Springer, 1992.
- [22] E.S. Fedorov. Symmetry in the plane. In *Zapiski Imperatorskogo S. Peterburgskogo Mineralogicheskogo Obshchestva [Proc. S. Peterb. Mineral. Soc.]*, volume 2, pages 345–390, 1891.
- [23] W. Friedrich, P. Knipping, and M. Laue. Interferenzerscheinungen bei roentgenstrahlen. *Annalen der Physik*, 346(10):971–988, 1913.
- [24] M.G.L. Gustafsson. Surpassing the lateral resolution limit by a factor of two using structured illumination microscopy. *Journal of microscopy*, 198(2):82–87, 2000.
- [25] T.C. Harman, P.J. Taylor, M.P. Walsh, and B.E. LaForge. Quantum dot superlattice thermoelectric materials and devices. *science*, 297(5590):2229–2232, 2002.
- [26] W.M. Haynes. *CRC handbook of chemistry and physics*. CRC press, 2014.
- [27] J. Hays, M. Leordeanu, A.A. Efros, and Y. Liu. Discovering texture regularity as a higher-order correspondence problem. In *European Conference on Computer Vision*, pages 522–535. Springer, 2006.
- [28] C.G. Healey and J.T. Enns. Building perceptual textures to visualize multidimensional datasets. In *Visualization’98. Proceedings*, pages 111–118. IEEE, 1998.
- [29] H. Hiller. Crystallography and cohomology of groups. *The American Mathematical Monthly*, 93(10):765–779, 1986.

- [30] Petri Hirvonen, Gabriel Martine La Boissonière, Zheyong Fan, Cristian-Vasile Achim, Nikolas Provatas, Ken R Elder, and Tapio Ala-Nissila. Grain extraction and microstructural analysis method for two-dimensional poly and quasicrystalline solids. *arXiv preprint arXiv:1806.00700*, 2018.
- [31] J.L. Hock and R.B. McQuistan. The occupation statistics for indistinguishable dumbbells on a $2 \times 2 \times N$ lattice space. *Journal of Mathematical Physics*, 24(7):1859–1865, 1983.
- [32] S. Horbelt, M. Liebling, and M. Unser. Discretization of the radon transform and of its inverse by spline convolutions. *IEEE Transactions on medical imaging*, 21(4):363–376, 2002.
- [33] M.K. Jana and C.N.R. Rao. Two-dimensional inorganic analogues of graphene: transition metal dichalcogenides. *Phil. Trans. R. Soc. A*, 374(2076):20150318, 2016.
- [34] C.H. Johansson and J.O. Linde. Röntgenographische bestimmung der atomanordnung in den mischkristallreihen auCu und PdCu. *Annalen der Physik*, 383(21):439–460, 1925.
- [35] B. Julesz. Textons, the elements of texture perception, and their interactions. *Nature*, 290(5802):91, 1981.
- [36] A. Korkine and G. Zolotareff. Sur les formes quadratiques. *Mathematische Annalen*, 6(3):366–389, 1873.
- [37] A. Kudrolli, B. Pier, and J.P. Gollub. Superlattice patterns in surface waves. *Physica D: nonlinear phenomena*, 123(1-4):99–111, 1998.
- [38] A.K. Lenstra, H.W. Lenstra, and L. Lovász. Factoring polynomials with rational coefficients. *Mathematische Annalen*, 261(4):515–534, 1982.
- [39] T. Leung and J. Malik. Detecting, localizing and grouping repeated scene elements from an image. In *European Conference on Computer Vision*, pages 546–555. Springer, 1996.
- [40] Jianfeng Lu and Haizhao Yang. Phase-space sketching for crystal image analysis based on synchrosqueezed transforms. *SIAM Journal on Imaging Sciences*, 11(3):1954–1978, 2018.
- [41] T. Matsuyama, S. Miura, and M. Nagao. Structural analysis of natural textures by fourier transformation. *Computer vision, graphics, and image processing*, 24(3):347–362, 1983.
- [42] H. Minkowski. Geometrie der zahlen. *Bull. Amer. Math. Soc.*
- [43] H. Minkowski. Über die positiven quadratischen formen und über kettenbruchähnliche algorithmen. *J. Reine und Angewandte Math*, 107:278–297.
- [44] T.D. Musho and D.G. Walker. Thermoelectric properties of superlattice materials with variably spaced layers. *Journal of Materials Research*, 26(15):1993–2000, 2011.
- [45] D.K. Naidu and R.B. Fisher. A comparative analysis of algorithms for determining the peak position of a stripe to sub-pixel accuracy. In *BMVC91*, pages 217–225. Springer, 1991.
- [46] H. Nobach and M. Honkanen. Two-dimensional gaussian regression for sub-pixel displacement estimation in particle image velocimetry or particle position estimation in particle tracking velocimetry. *Experiments in fluids*, 38(4):511–515, 2005.

- [47] K.S. Novoselov, A.K. Geim, S.V. Morozov, D.A. Jiang, Y. Zhang, S.V. Dubonos, I.V. Grigorieva, and A.A. Firsov. Electric field effect in atomically thin carbon films. *science*, 306(5696):666–669, 2004.
- [48] N. Otsu. A threshold selection method from gray-level histograms. *IEEE transactions on systems, man, and cybernetics*, 9(1):62–66, 1979.
- [49] M. Park, K. Brocklehurst, R.T. Collins, and Y. Liu. Deformed lattice detection in real-world images using mean-shift belief propagation. *IEEE Transactions on Pattern Analysis and Machine Intelligence*, 31(10):1804–1816, 2009.
- [50] D.P. Petersen and D. Middleton. Sampling and reconstruction of wave-number-limited functions in N-dimensional euclidean spaces. *Information and control*, 5(4):279–323, 1962.
- [51] E. Picard. *Oeuvres de Charles Hermite*. 1905.
- [52] C.N.R. Rao, U. Maitra, and U.V. Waghmare. Extraordinary attributes of 2-dimensional MoS_2 nanosheets. *Chemical Physics Letters*, 609:172–183, 2014.
- [53] C.N.R. Rao, M.H. Ramakrishna, and U. Maitra. Graphene analogues of inorganic layered materials. *Angewandte Chemie International Edition*, 52(50):13162–13185, 2013.
- [54] C.A. Rogers. Mean values over the space of lattices. *Acta mathematica*, 94(1):249–287, 1955.
- [55] F. Schaffalitzky and A. Zisserman. Geometric grouping of repeated elements within images. In *Shape, Contour and Grouping in Computer Vision*, pages 165–181. Springer, 1999.
- [56] L.I. Schiff. Lattice-space quantization of a nonlinear field theory. *Physical Review*, 92(3):766, 1953.
- [57] C.L. Siegel. *Lectures on the Geometry of Numbers*. Springer Science & Business Media, 2013.
- [58] M. Silber, C.M. Topaz, and A.C. Skeldon. Two-frequency forced faraday waves: weakly damped modes and pattern selection. *Physica D: nonlinear phenomena*, 143(1-4):205–225, 2000.
- [59] C. Sun. Fast optical flow using 3D shortest path techniques. *Image and vision computing*, 20(13-14):981–991, 2002.
- [60] G.P. Thomson and A. Reid. Diffraction of cathode rays by a thin film. *Nature*, 119(3007):890, 1927.
- [61] B. Vallée and A. Vera. Lattice reduction in two dimensions: analyses under realistic probabilistic models. 2008.
- [62] D. Voiry, A. Mohite, and M. Chhowalla. Phase engineering of transition metal dichalcogenides. *Chemical Society Reviews*, 44(9):2702–2712, 2015.
- [63] C. Weigle, W.G. Emigh, G. Liu, R.M. Taylor, J.T. Enns, and C.G. Healey. Oriented texture slivers: A technique for local value estimation of multiple scalar fields. In *Proceedings Graphics Interface*, pages 163–170, 2000.

- [64] E.G. Westhoff, V. Kneisel, Y.A. Logvin, T. Ackemann, and W. Lange. Pattern formation in the presence of an intrinsic polarization instability. *Journal of Optics B: Quantum and Semiclassical Optics*, 2(3):386, 2000.
- [65] J.M. Wolfe, K.R. Cave, and S.L. Franzel. Guided search: an alternative to the feature integration model for visual search. *Journal of Experimental Psychology: Human perception and performance*, 15(3):419, 1989.
- [66] H. Wu, K.W.J. Malafant, L.K. Pendridge, P.J.H. Sharpe, and J. Walker. Simulation of two-dimensional point patterns: application of a lattice framework approach. *Ecological Modelling*, 38(3-4):299–308, 1987.
- [67] P. Yashar, S.A. Barnett, J. Rechner, and W.D. Sproul. Structure and mechanical properties of polycrystalline *CrN/TiN* superlattices. *Journal of Vacuum Science & Technology A: Vacuum, Surfaces, and Films*, 16(5):2913–2918, 1998.
- [68] Y.Liu, R.T. Collins, and Y. Tsin. A computational model for periodic pattern perception based on frieze and wallpaper groups. *IEEE Transactions on Pattern Analysis & Machine Intelligence*, (3):354–371, 2004.
- [69] J. Zheng, H. Zhang, S. Dong, Y. Liu, C. Nai, H.S. Shin, H.Y. Jeong, B. Liu, and K.P. Loh. High yield exfoliation of two-dimensional chalcogenides using sodium naphthalenide. *Nature communications*, 5:2995, 2014.
- [70] Dominique Zosso, Konstantin Dragomiretskiy, Andrea L Bertozzi, and Paul S Weiss. Two-dimensional compact variational mode decomposition. *Journal of Mathematical Imaging and Vision*, 58(2):294–320, 2017.